Inorg. Chem. **2003**, *42*, 2606–2621

Inorganic Chemistry

Article

Structure, Stability, and Electronic and NMR Properties of Various Oxo- and Nitrido-Derivatives of [L(Salen)Mn(III)]$^+$, Where L = None and Imidazole. A Density Functional Study

Ilja V. Khavrutskii, Djamaladdin G. Musaev,* and Keiji Morokuma*

Cherry L. Emerson Center for Scientific Computation and Department of Chemistry,
Emory University, Atlanta, Georgia 30322

Received October 8, 2002

Structure, stability, and electronic and NMR properties of [(Salen)Mn(III)]$^+$-derived intermediates/reactants in the epoxidation/amination of unfunctionalized olefins, namely [(Salen)Mn(V)O]$^+$ (**1-oxo**), [(Salen)Mn(IV)O] (**2-oxo**), and [(Salen)Mn(V)N] (**3**), have been studied with the B3LYP density functional method. It has been shown that the ^{1}**A**, ^{3}**A**, and ^{5}**A** states of cationic **1-oxo** species are virtually degenerate, while for the neutral **2-oxo** species the ground ^{4}**A** state lies 6.4 kcal/mol lower than ^{2}**A**. In the nitrido species **3**, the ^{1}**A** state has been shown to be the ground state in agreement with experiment. We have investigated isomerization of **1-oxo** and **2-oxo** species into unusual [(OSalen)Mn(III)]$^+$ (**1-N-oxo** and **1-peroxo**) and [(OSalen)Mn(II)] (**2-N-oxo** and **2-peroxo**) species, respectively. For cationic species **1**, the **1-N-oxo** isomers are more stable (by 10–12 kcal/mol) than the **1-oxo** isomer and are separated from the latter by 21–22 kcal/mol barriers. On the other hand, **1-peroxo** isomers are calculated to be 14–16 kcal/mol higher than the **1-oxo** isomer. For neutral species **2**, however, both **2-N-oxo** and **2-peroxo** isomers lie significantly higher in energy than the **2-oxo** isomer. It has been shown that coordination of axial imidazole ligand alters relative energies of spin states for **1-** and **2-oxo** species, destabilizing low-spin states. For singlet states of H_2Salen, **1-oxo**, and **3**, we have calculated ^{1}H, ^{13}C, ^{15}N, and ^{17}O NMR chemical shifts using the gauge-independent-atomic orbital (GIAO) approach.

I. Introduction

The discovery of the catalytically active *N*,*N*-ethylenebis(salycildeneaminato) Mn(III) cationic complex, [(Salen)Mn(III)]$^+$, by Kochi,[1,2] Jacobsen,[3-5] and Katsuki[6-8] (KJK) for the epoxidation of olefins with a variety of oxidants provided an exceptionally versatile and highly enantioselective method in organic synthesis. The KJK system is superior in enantioselectivity of epoxidation to its porphyrin analogues, models for cytochrome P-450,[7,9] and has attracted considerable interest. Numerous experimental studies have demonstrated that [(Salen)Mn(III)]$^+$-derived species can

---

* Corresponding authors. E-mail: dmusaev@emory.edu (D.G.M.); morokuma@emory.edu (K.M.).

(1) Srinivasan, K.; Michaud, P.; Kochi, J. K. *J. Am. Chem. Soc.* **1986**, *108*, 2309−2320.

(2) Srinivasan, K.; Perrier, S.; Kochi, J. K. *J. Mol. Catal.* **1986**, *36*, 297−317.

(3) Zhang, W.; Loebach, J. L.; Wilson, S. R.; Jacobsen, E. N. *J. Am. Chem. Soc.* **1990**, *112*, 2801−2803. Jacobsen, E. N.; Zhang, W.; Muci, A. R.; Ecker, J. R.; Deng, L. *J. Am. Chem. Soc.* **1991**, *113*, 7063−7064. Zhang, W.; Jacobsen, E. N. *J. Org. Chem.* **1991**, *56*, 2296−2298. Palucki, M.; Hanson, P.; Jacobsen, E. N. *Tetrahedron Lett.* **1992**, *33*, 7111−7114. Li, Z.; Conser, K. R.; Jacobsen, E. N. *J. Am. Chem. Soc.* **1993**, *115*, 5326−5327. Palucki, M.; Pospisil, P. J.; Zhang, W.; Jacobsen, E. N. *J. Am. Chem. Soc.* **1994**, *116*, 9333−9334. Zhang, W.; Lee, N. H.; Jacobsen, E. N. *J. Am. Chem. Soc.* **1994**, *116*, 425−426. Palucki, M.; McCormick, G. J.; Jacobsen, E. N. *Tetrahedron Lett.* **1995**, *36*, 5457−5460. Pospisil, P. J.; Carsten, D. H.; Jacobsen, E. N. *Chem.*−*Eur. J.* **1996**, *2*, 974−980.

(4) Jacobsen, E. N.; Zhang, W.; Guler, M. L. *J. Am. Chem. Soc.* **1991**, *113*, 7063−7064. Jacobsen, E. N. In *Catalytic Asymmetric Synthesis*, 1st ed.; Ojima, I., Ed.; VCH Publishers: New York, 1993; pp 159−202.

(5) Jacobsen, E. N.; Wu, M. H. In *Comprehensive Asymmetric Catalysis: Asymmetric synthesis and induction Catalysts*; Jacobsen, E. N., Pfaltz, A., Yamamoto, H., Eds.; Springer: New York, 1999; Vol. 2, pp 649−677.

(6) Irie, R.; Noda, K.; Ito, Y.; Matsumoto, N.; Katsuki, T. *Tetrahedron Lett.* **1990**, *31*, 7345−7348. Irie, R.; Noda, K.; Ito, Y.; Katsuki, T. *Tetrahedron Lett.* **1991**, *32*, 1055−1058. Irie, R.; Ito, Y.; Katsuki, T. *Synlett* **1991**, 265−266. Irie, R.; Noda, K.; Ito, Y.; Matsumoto, N.; Katsuki, T. *Tetrahedron*: *Asymmetry* **1991**, *2*, 481−944. Noda, K.; Hosoya, N.; Irie, R.; Ito, Y.; Katsuki, T. *Synlett* **1993**, 7. Katsuki, T. *J. Mol. Catal. A: Chem.* **1996**, *113*, 87−107.

(7) Katsuki, T. *Coord. Chem. Rev.* **1995**, *140*, 189−214.

(8) Katsuki, T. In *Catalytic Asymmetric Synthesis*, 2nd ed.; Ojima, I., Ed.; Wiley-VCH: New York, 2000; pp 287−325.

(9) Collman, J. P.; Zhang, X.; Lee, V. J.; Uffelman, E. S.; Brauman, J. I. *Science (Washington, D.C.)* **1993**, *261*, 1404−1411.

10.1021/ic026094q CCC: $25.00

Scheme 1. Studied Isomers of the Cationic **1-Oxo** and Neutral **2-Oxo** Species[a]

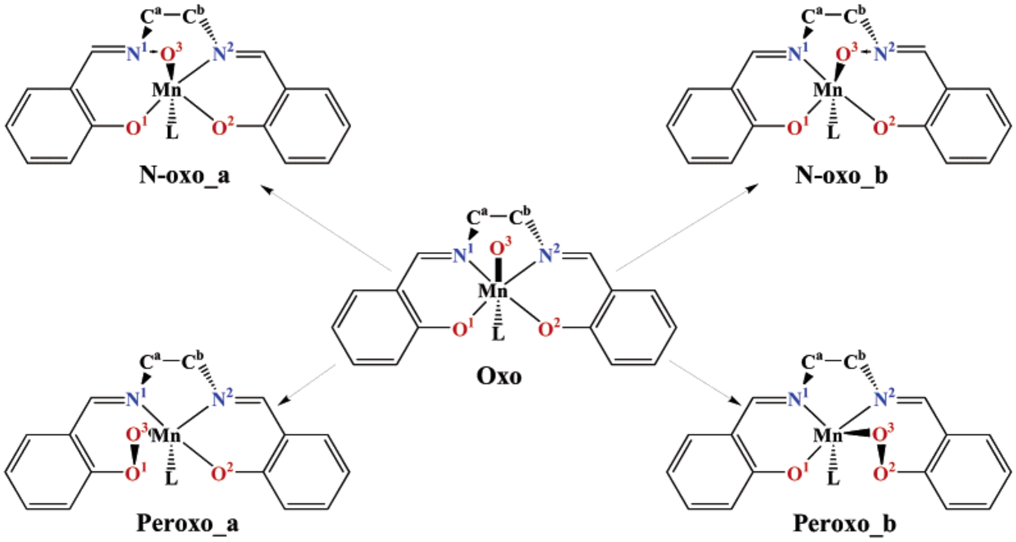

[a] Here, L = none or imidazole (Imd).

easily oxidize and aminate alkenes,[5,8,10−12] while the nature and identity of the reactive species still need to be elucidated. On the basis of the similarity to their porphyrin analogues, where the active species in epoxidation is commonly believed to be the metal−oxo compound,[13−15] Kochi has postulated the cationic oxo-species [(Salen)Mn(V)O]$^+$ (**1-oxo**) to be the active oxidant in the KJK reactions.[1] This idea has been supported by the characterization of the [(Salen)Cr(V)O]$^+$ complex[16] and has been further substantiated by characterization of the isoelectronic complex [(Salen)Mn(V)N] (**3**),[10−12,17,18] analogous to that of porphyrins.[19] Although claims of detecting [(Salen)Mn(V)O]$^+$ species have been made recently by ^{1}H NMR[20] and ESMS[21−24] techniques, both experiments have deficiencies. In the ^{1}H NMR studies, the authors assumed that both species **1-oxo** and **3** have a singlet ground state and that their NMR spectra are alike, whereas in the ESMS detection, the existence of other species, such as the **N-oxo** form of species **1** (**1-N-oxo**, see Scheme 1 and following paragraphs for notations used in this paper), with an m/z ratio equal to that of **1-oxo**, has not even been considered. It is worth noting that the species similar to **1-N-oxo** have been earlier suggested[25] and later characterized experimentally for the nickel porphyrins,[26] both experimentally[14,27] and theoretically[28] for the iron porphyrins, and only theoretically for manganese complexes.[29] In the latter case, tentatively the **1-N-oxo** complex has been structurally characterized by EXAFS/XANES methods.[30]

Furthermore, several research teams recently have paid attention to the conversion of the cationic [(Salen)Mn(V)O]$^+$ oxo species (**1-oxo**) to the neutral species [(Salen)Mn(IV)O] (**2-oxo**) in the absence of substrate,[20,31−34] analogous to the porphyrin case.[15,35] It has been shown that **2-oxo** is relatively

---

(10) Neely, F. L.; Bottomley, L. A. *Inorg. Chim. Acta* **1992**, *192*, 147−149. Chang, C. J.; Low, D. W.; Gray, H. B. *Inorg. Chem.* **1997**, *36*, 270−271.

(11) Du Bois, J.; Hong, J.; Carreira, E. M.; Day, M. W. *J. Am. Chem. Soc.* **1996**, *118*, 915−916.

(12) Du Bois, J.; Tomooka, C. S.; Hong, J.; Carreira, E. M. *Acc. Chem. Res.* **1997**, *30*, 364−372.

(13) Groves, J. T.; Nemo, T. E.; Myers, R. S. *J. Am. Chem. Soc.* **1979**, *101*, 1032−1033. Groves, J. T.; Watanabe, Y. *J. Am. Chem. Soc.* **1986**, *108*, 7834−7836. Groves, J. T.; Watanabe, Y. *J. Am. Chem. Soc.* **1986**, *108*, 507−508. Groves, J. T.; Lee, J.; Marla, S. S. *J. Am. Chem. Soc.* **1997**, *119*, 6269−6273. Groves, J. T.; Kruper, W. J.; Nemo, T. E.; Myers, R. S. *J. Mol. Catal.* **1980**, *7*, 169−177. Groves, J. T.; Kruper, W. J., Jr.; Haushalter, R. C. *J. Am. Chem. Soc.* **1980**, *102*, 6375−6377. Groves, J. T. *J. Porphyrins Phthalocyanines* **2000**, *4*, 350−352.

(14) Groves, J. T.; Nemo, T. E. *J. Am. Chem. Soc.* **1983**, *105*, 5786−5791. Groves, J. T.; Watanabe, Y. *J. Am. Chem. Soc.* **1988**, *110*, 8443−8452.

(15) Groves, J. T.; Stern, M. K. *J. Am. Chem. Soc.* **1988**, *110*, 8628−8638.

(16) Siddall, T. L.; Miyaura, N.; Huffman, J. C.; Kochi, J. K. *J. Chem. Soc., Chem. Commun.* **1983**, 1185−1186. Samsel, E. G.; Srinivasan, K.; Kochi, J. K. *J. Am. Chem. Soc.* **1985**, *107*, 7606−7617. Srinivasan, K.; Kochi, J. K. *Inorg. Chem.* **1985**, *24*, 4671−4679.

(17) Chang, C. J.; Connick, W. B.; Low, D. W.; Day, M. W.; Gray, H. B. *Inorg. Chem.* **1998**, *37*, 3107−3110.

(18) Jepsen, A. S.; Roberson, M.; Hazell, R. G.; Jorgensen, K. A. *Chem. Commun.* **1998**, 1599−1600.

(19) Hill, C. L.; Hollander, F. J. *J. Am. Chem. Soc.* **1982**, *104*, 7318−7319.

(20) Bryliakov, K. P.; Babushkin, D. E.; Talsi, E. P. *J. Mol. Catal. A: Chem.* **2000**, *158*, 19−35.

(21) Feichtinger, D.; Plattner, D. A. *Angew. Chem., Int. Ed. Engl.* **1997**, *36*, 1718−1719.

(22) Plattner, D. A.; Feichtinger, D.; El-Bahraoui, J.; Wiest, O. *Int. J. Mass Spectrom.* **2000**, *195*/*196*, 351−362.

(23) Feichtinger, D.; Plattner, D. A. *Perkin 2 (2000)* **2000**, *5*, 1023−1028.

(24) Feichtinger, D.; Plattner, D. A. *Chem.*−*Eur. J.* **2001**, *7*, 591−599.

(25) Tatsumi, K.; Hoffman, R. *Inorg. Chem.* **1981**, *20*, 3771−3784.

(26) Balch, A. L.; Chan, Y.-W.; Olmstead, M. M. *J. Am. Chem. Soc.* **1985**, *107*, 6510−6514.

(27) Groves, J. T.; Watanabe, Y. *J. Am. Chem. Soc.* **1986**, *108*, 24.

(28) Strich, A.; Veillard, A. *Nouv. J. Chim.* **1983**, *7*, 347−352. Jorgensen, K. A. *Acta Chem. Scand., Ser. B* **1986**, *40*, 512−514. Jorgensen, K. A. *J. Am. Chem. Soc.* **1987**, *109*, 698−705.

(29) Den Boer, D. H. W.; Van der Made, A. W.; Zwaans, R.; Van Lenthe, J. H. *Recl. Trav. Chim. Pays-Bas* **1990**, *109*, 123−126.

(30) Bortolini, O.; Meunier, B. *J. Chem. Soc., Chem. Commun.* **1983**, 1364−1366. Bortolini, O.; Ricci, M.; Meunier, B.; Friant, P.; Ascone, I.; Goulon, J. *Nouv. J. Chim.* **1986**, *10*, 39−49.

(31) Bryliakov, K. P.; Khavrutskii, I. V.; Talsi, E. P.; Kholdeeva, O. A. *React. Kinet. Catal. Lett.* **2000**, *71*, 183−191.

(32) Adam, W.; Mock-Knoblauch, C.; Saha-Moeller, C. R.; Herderich, M. *J. Am. Chem. Soc.* **2000**, *122*, 9685−9691.

(33) Campbell, K. A.; Lashley, M. R.; Wyatt, J. K.; Nantz, M. H.; Britt, R. D. *J. Am. Chem. Soc.* **2001**, *123*, 5710−5719.

(34) Bryliakov, K. P.; Kholdeeva, O. A.; Vanina, M. P.; Talsi, E. P. *J. Mol. Catal. A: Chem.* **2002**, *178*, 47−53.

(35) Smegal, J. A.; Hill, C. L. *J. Am. Chem. Soc.* **1983**, *105*, 3515−3521.

stable, exhibits characteristic ESR spectrum, and oxidizes olefins via a stepwise radical mechanism.[20,32] Although the accumulation of **2-oxo** in the presence of substrate is unlikely, such species could certainly play an important role at high conversion and with rigid substrates. In addition to monomeric species, several dimers such as Mn(III)Mn(IV) and Mn(IV)Mn(IV) have been reported to be involved in the reaction as well.[1,2,20,22−24,31,36] Thus, a number of species besides **1-oxo** could form in the reaction conditions and should be taken into account in interpretation of experimental data.

The studies of structural properties of all active species could be essential for an understanding of the overall reaction mechanism. As proposed by Groves and Myers[37] on the basis of Fe−porphyrin systems, the structural properties of the active species can reveal the factors controlling the stereoselectivity of the epoxidation reaction. However, up to now, no structural information is experimentally available for the putative **1-oxo**. An estimate of its geometry mainly has been obtained from the X-ray data of $[(\mathrm{Salen})\mathrm{Cr(V)O}]^{+}$ [16] and complex **3**.[10−12,17,18]

Another essential aspect for understanding the mechanism of the epoxidation reaction is the electronic structure of the active species and how the electronic structure is affected by coordination of axial ligands.[1,4,7,38] Indeed, knowledge of electronic structure of the active species is crucial for understanding the nature of the terminal Mn−O/N bonds in species **1-oxo**, **2-oxo**, and **3**, and their reactivity. However, due to the unstable nature of many of the expected reactive intermediates, the experiments are limited to the determination of high spin ($S = 2$) for the parent complex $[(\mathrm{Salen})\mathrm{Mn(III)}]^{+}$,[33,39] high spin ($S = {}^{3}/_{2}$) for **2-oxo**,[20,32,33] and low spin ($S = 0$) for species **3**.[11,17]

In elucidating the geometric and electronic structures of the transient intermediates, one of the best approaches is the quantum chemical calculation. Recently, several density functional studies on the geometric and electronic structures of the complex **1-oxo** and singlet ground state of **3** have been published.[18,22,24,40−44] In these studies, two models, **model_I** and **model_II**, depicted in Scheme 2 (where X stands for oxygen or nitrogen terminal atoms, while L refers to its trans ligand), have been used. The **model_I** species represents the conjugated core of the Salen ligand and is missing the two benzene rings, whereas **model_II** delineates the full Salen ligand.

Let us briefly discuss the results from previous studies summarized in Table 1. For the cationic complex $[(\mathrm{Salen})\mathrm{Mn(V)O}]^{+}$, **model_I** (X = O; L = none), Linde found the triplet state to be the ground state, with singlet and quintet states lying 1.4 and 2.6 kcal/mol higher, respectively.[40] The terminal Mn−O bond length is calculated to be 1.62 and 1.71 Å in the triplet and quintet states, respectively. Unfortunately, the authors did not provide the Mn−O bond length for the singlet state. Jepsen et al. have studied the singlet state of cationic complex $[(\mathrm{Salen})\mathrm{Mn(V)O}]^{+}$, **model_I** (X = O; L = none), merely for comparison with isoelectronic nitrido species **3**, **model_I** (X = N, L = none), and found the Mn−O bond length to be 1.55 Å.[18] On the other hand, using the same B3LYP functional with slightly better all-electron basis sets, Strassner et al.[41] have reported the singlet ground state for the cationic $[(\mathrm{Salen})\mathrm{Mn(V)O}]^{+}$ (**1-oxo**) complex with the triplet and quintet states lying 3.5 and 11.2 kcal/mol higher, respectively. For the neutral [Cl(Salen)Mn(V)O] complex **1-Cl⁻-oxo**, **model_I** (X = O, L = Cl^{-}), they have reported a spin-contaminated triplet ($\langle S^{2}\rangle = 2.9$) ground state, with the singlet and quintet lying 10.2 and 2.0 kcal/mol higher, respectively. Unfortunately, these authors do not provide any geometrical parameters for the corresponding complexes. Comparison of these results for cationic and neutral systems shows that trans ligand Cl^{-} significantly destabilizes low-spin states, especially the singlet state. Cavallo et al.[43] have reported similar results for the neutral complex **1-Cl⁻-oxo** using the same model as Strassner et al., but with the BP86 (see later) nonhybrid density functional with Slater type basis sets. They have shown that the triplet state is the ground state with terminal Mn−O bond length of 1.64 Å. The quintet state is calculated to be 10.8 kcal/mol higher in energy and have 1.78 Å Mn−O bond length. The comparison of results from Strassner et al. and Cavallo et al. on the energy gap between the triplet and quintet states (2.0 and 10.8 kcal/mol, respectively) shows that the BP86 method significantly overestimates the energies of high-spin states compared to B3LYP, which is consistent with our previous conclusion.[45]

Scheme 2. Truncated (**Model_I**) and Full (**Model_II**) Salen Computational Models Used in the Literature[a]

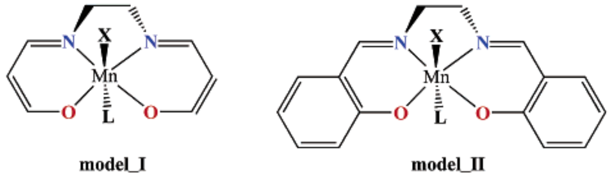

[a] In the present study, **model_II** is used, with X = O (cationic and neutral species **1** and **2**, respectively) and N (species **3**), and L = none or imidazole (Imd).

For a more realistic model, **model_II** (X = O, L = none), Plattner et al. have studied the singlet, triplet, and quintet states of the cationic **1-oxo** species using a triple-ζ quality basis set.[22] They have found the singlet ground state with the terminal Mn−O bond length of 1.52 Å. The triplet and quintet states lie 0.9 and 7.7 kcal/mol higher and have the terminal Mn−O bond lengths of 1.58 and 1.65 Å, respectively. Comparison of the obtained Mn−O bond distances

---

(36) Bryliakov, K. P.; Babushkin, D. E.; Talsi, E. P. *Mendeleev Commun.* **2000**, *1*, 1−3.

(37) Groves, J. T.; Myers, R. S. *J. Am. Chem. Soc.* **1983**, *105*, 5791−5796.

(38) Palucki, M.; Finney, N. S.; Pospisil, P. J.; Gueler, M. L.; Ishida, T.; Jacobsen, E. N. *J. Am. Chem. Soc.* **1998**, *120*, 948−954.

(39) Bryliakov, K. P.; Babushkin, D. E.; Talsi, E. P. *Mendeleev Commun.* **1999**, *1*, 29−32.

(40) Linde, C.; Aakermark, B.; Norrby, P.-O.; Svensson, M. *J. Am. Chem. Soc.* **1999**, *121*, 5083−5084.

(41) Strassner, T.; Houk, K. N. *Org. Lett.* **1999**, *1*, 419−421.

(42) El-Bahraoui, J.; Wiest, O.; Feichtinger, D.; Plattner, D. A. *Angew. Chem., Int. Ed.* **2001**, *40*, 2073−2076.

(43) Cavallo, L.; Jacobsen, H. *Angew. Chem., Int. Ed.* **2000**, *39*, 589−592.

(44) Jacobsen, H.; Cavallo, L. *Chem.*−*Eur. J.* **2001**, *20*, 1533−1544.

(45) Khoroshun, D. V.; Musaev, D. G.; Vreven, T.; Morokuma, K. *Organometallics* **2001**, *20*, 2007−2026.

Table 1. Relative Energies, Terminal MnO Bond Distances, and $\langle \mathbf{S}^2 \rangle$ Values for the Low-Lying Electronic States of the Species **1-Oxo** Calculated for **Model_II** with Different Methods with the BS2[a] and Compared with Previous Theoretical Results

method	ref	L	^{1}A-R[a]	^{1}A-U[a]	^{3}A	^{5}A
			Relative Energy (kcal/mol)			
model-II: HF[b]	present work	none	0.0	−9.1	−127.7	−105.7
model-II, B3LYP[b]	present work	none	0.0	−0.6	−1.5	0.5
model-II, B3P86[b]	present work	none	0.0	−1.0	−1.2	3.0
model-II, BLYP[b]	present work	none	0.0	−0.1	2.5	13.8
model-II, BP86[b]	present work	none	0.0	−0.1	2.9	16.5
model-II, B3LYP[b]	present work	Imd	0.0	−2.3	−14.3	−14.0
model_I, B3LYP[c]	Linde et al.	none	0.0		−1.4	1.2
model_I, B3LYP[d]	Strassner et al.	none	0.0		3.5	11.2
model_I, B3LYP[d]	Strassner et al.	Cl^-	0.0		−10.2	−8.2
model_I, BP86[e]	Cavallo et al.	Cl^-			0.0	10.8
model_II, B3LYP[f]	Plattner et al.	none	0.0		0.9	7.7
model_II, B3LYP[f]	Plattner et al.	CH_3CN			0.0	0.5
model_II, B3LYP[f]	Plattner et al.	$(CH_3)_3NO$	0.0		−10.8	−7.8
model_I, BP86[g]	Abashkin et al.	Cl^-		0.0	6.7	17.6
			Terminal Mn−O (Å)			
model-II, B3LYP[b]	present work	none		1.55	1.62	1.68
model-II, B3LYP[b]	present work	Imd	1.56	1.60	1.78	1.75
model_I, B3LYP[c]	Linde et al.	none			1.62	1.71
model_I, B3LYP[h]	Jepsen et al.	none	1.55			
model_I, B3LYP[h]	Jepsen et al.	Cl^-	1.55			
model_I, BP86[e]	Cavallo et al.	Cl^-			1.64	1.78
model_II, B3LYP[f]	Plattner et al.	none	1.52		1.57	1.65
model_II, B3LYP[f]	Plattner et al.	CH_3CN			1.60	1.68
model_II, B3LYP[f]	Plattner et al.	$(CH_3)_3NO$	1.53		1.71	1.74
model_I, BP86[g]	Abashkin et al.	Cl^-	1.58		1.65	1.76
			$\langle \mathbf{S}^2 \rangle$			
model-II, HF[b]	present work	none	0.00	0.78	3.60	6.98
model-II, B3LYP[b]	present work	none	0.00	0.31	2.31	6.06
model-II, B3P86[b]	present work	none	0.00	0.37	2.30	6.06
model-II, BLYP[b]	present work	none	0.00	0.05	2.06	6.03
model-II, BP86[b]	present work	none	0.00	0.02	2.05	6.03
model_I, B3LYP[d]	Strassner et al.	none	0.00		2.10	6.10
model_I, B3LYP[d]	Strassner et al.	Cl^-			2.90	6.10
model_II, B3LYP[f]	Plattner et al.	none	0.00		2.10	6.05
model_II, B3LYP[f]	Plattner et al.	CH_3CN			2.21	6.05
model_II, B3LYP[f]	Plattner et al.	$(CH_3)_3NO$	0.00		2.81	6.05

[a] R and U stand for restricted and unrestricted methods, respectively. [b] Energies and $\langle \mathbf{S}^2 \rangle$ values are calculated using the BS2 basis set (Mn, (8s7p6d1f)/[6s5p3d1f] with associated Stuttgart−Dresden ECP; C, N, O, (12s6p1d)/[5s5p1d]; H, (5)/[3]) at the B3LYP/BS1 optimized geometries. [c] Ref 40. Basis set: Mn, (14s11p6d)/[6s5p3d]; C, N, O, (9s5p)/[4s2p]; H, (4s)/[2s]. [d] Ref 41. Basis set: Mn, (17s10p6d)/[6s3p3d]; Cl, (16s10p1d)/[4s3p1d]; C, N, O, (10s4p1d)/[3s2p1d]; H, (4s)/[2s]. [e] Ref 43. Basis set: Mn, triple-ζ STO(p); Cl, C, N, O, H, double-ζ STO(p). [f] Ref 22 and 42. Basis set: Mn, (14s9p5d1f)/[9s5p3d1f]; C, N, O, (11s5p1d)/[4s3p1d]; H, (5s)/[3s]. [g] Ref 46. Basis set: Mn, (15s9p5d)/[5s3p2d]; Cl, (12s8p1d)/[4s3p1d]; C, N, O, (9s5p1d)/[3s2p1d]; H, (5s)/[2s]. [h] Ref 18. Basis set: same as footnote d.

by Plattner et al. (**model_II**) and Linde et al. (**model_I**), where both authors used B3LYP, shows that the Mn−O bond lengths are significantly (0.04 and 0.06 Å, for triplet and quintet states, respectively) shorter in the former model.

When this paper was in preparation, Abashkin and co-workers[46] published an interesting paper on the electronic and geometrical structures of the cationic **1-oxo** and neutral **1-Cl$^-$-oxo** complexes, as well as ethylene epoxidation by the latter complexes using **model_I**. In this paper, the authors used the BP86 method with a valence-double-ζ quality basis set (for C, N, and O atoms, the polarization d-functions also were added) for geometry optimization. On the basis of their BP86 and single point (at the BP86 optimized geometries) B3LYP and CCSD(T) (using truncated model and basis sets) calculations, the authors have concluded that (1) the BP86 method provides “a realistic description of the relations between the different spin channels involved in the reaction”, and (2) “using the B3LYP approach in this particular catalytic system case results in a distorted picture of the spin state order”. However, the detailed analysis of the presented data indicates that the authors do not have enough evidence for such definite conclusions. Indeed, (1) the data presented in the paper in its Table 1 for the SC (simplified cationic) model shows that the CCSD(T) results are not converged with respect to the basis sets; relative energies of the different electronic states change by 4−5 kcal/mol upon improving basis sets from valence double-ζ plus polarization (DZVPc) to valence triple-ζ plus polarization (TZVPc), where c refers to DZ for H and C atoms.

(2) The differences between CCSD(T) and BP86 results are significantly larger (11.3 and 16.3 kcal/mol for triplet and quintet states, respectively) than those between CCSD-(T) and B3LYP (which 3.0 and 12.3 kcal/mol for triplet and quintet states, respectively).

(3) At both BP86 and B3LYP levels of calculations, the triplet and quintet states are stabilized by 6−7 and 14−16 kcal/mol, respectively, relative to the singlet state upon going

---

(46) Abashkin, Y. G.; Collins, J. R.; Burt, S. K. *Inorg. Chem.* **2001**, *40*, 4040−4048.

from cationic (SC-model) to neutral (SN-model) systems. In contrast, at the CCSD(T) level, the triplet state is destabilized by 13 kcal/mol, while the quintet state is stabilized by 7 kcal/mol upon going from cationic (SC-model) to neutral (SN-model) systems. In other words, BP86 and B3LYP methods show similar trends upon going from cationic (SC-model) to neutral (SN-model) systems, while the limited CCSD(T) approach shows irregularity.

In order to elucidate the applicability of the BP86, BLYP, B3P86, B3LYP, and Hartree−Fock methods to the studies of the lower lying electronic states of complexes **1-oxo**, we have performed additional tests of the methods. The results of the extensive testing will be discussed in following sections.

In the present paper, we study structural and electronic properties of cationic oxo $[(Salen)Mn(V)O]^+$ (**1**), neutral oxo [(Salen)Mn(IV)O] (**2**), and nitrido species [(Salen)Mn(V)N] (**3**) using the B3LYP density functional method. Within **1** and **2**, we distinguish **oxo**, **N-oxo**, and **peroxo** isomers (see Scheme 1). As an axial ligand for our study, we chose imidazole over *N*-oxide, since imidazole is computationally more tractable, has been efficiently used by experimentalists,[47] does not necessarily undergo N-oxidation in the reaction conditions,[48] and exhibits all effects associated with axial ligand coordination without loss of generality.[31,34] We rationalize the characteristic structural properties of the species on the basis of their electronic structure. We also present ^{1}H, ^{13}C, ^{15}N, and ^{17}O NMR chemical shift results for the isoelectronic species **1-oxo** and **3**, as well as free H$_2$Salen and Salen^{2-}, and provide essential information for interpretation of the experimental results that is difficult to obtain otherwise.

In this work, we use the full Salen model, **model_II**, for oxo and nitrido species ($X = O$, N) with no axial ligand or imidazole axial ligand ($L =$ none and Imd). To refer to different spin states, we use the standard $^{2S+1}$A notation, where $2S + 1$ is multiplicity of the state and A is the symmetry of the total wave function.

II. Computational Methods

All calculations were performed with the Gaussian98 program suite.[49] For the present study, we used density functional theory (DFT), in particular unrestricted Becke three-parameter hybrid exchange functional (B3)[50,51] combined with Lee−Yang−Parr (LYP) correlation functional,[52] known as B3LYP. In addition, we used Becke88 (B) exchange functional[50] combined with Perdew86 (P86) correlation functional,[53] known as BP86. To make this comparison more systematic, we also employed two remaining combinations, BLYP and B3P86. Furthermore, to understand the origin of the difference between hybrid (B3LYP and B3P86) and pure (BLYP and BP86) density functionals, we performed single point calculations at the Hartree−Fock (HF) level.[54] In these calculations, the following basis sets were used: BS1, double-ζ quality basis set, comprised LANL2DZ (D95V[55]) basis set with associated Hay−Wadt nonrelativistic effective core potential (ECP) on the Mn[56] and Si atom;[57] BS2, triple-ζ quality basis set, comprised Stuttgart−Dresden (SDD) basis set (8s7p6d1f)/[6s5p3d1f] with associated ECPs for Mn[58] and (11s7p)/[6s4p] basis for Si atoms,[59] and 6-311+G(d) basis set[60] on the other atoms; and BS3 basis set, replacing 6-311+G(d) in BS2 by 6-311++G(d,p). Geometries of all compounds were optimized at the B3LYP/BS1 level. Unless stated otherwise, optimized structures were confirmed to be local minima by performing analytical harmonic vibrational frequency analysis. The energies were further refined by single point calculations at the B3LYP/BS2//B3LYP/BS1 level. For comparison of B3LYP, B3P86, BLYP, and BP86 functionals, we also performed DFT/BS2//B3LYP/BS1 single point calculations, where DFT = B3LYP, B3P86, BLYP, and BP86. Unless otherwise stated, we used unrestricted (U) method for all geometry optimizations, including singlet states. The spin contamination was monitored through the expectation value of $\mathbf{S}^2$. In addition, at the B3LYP/BS1 optimized geometries for the odd and even spin states, we performed single point restricted closed shell singlet (^{1}A//^{1}A, ^{1}A//^{3}A, and ^{1}A//^{5}A) and restricted doublet calculations (^{2}A//^{2}A and ^{2}A//^{4}A), respectively, using B3LYP/BS1 method, in order to analyze the molecular orbitals on equal footing. The molecular orbitals were visualized by Molden 3.6[61] and MOLEKEL 4.2.[62] The NMR chemical shifts were calculated for the closed shell singlet states of H$_2$Salen, Salen^{2-}, and compounds **1-oxo** and **3** using gauge-including atomic orbital (GIAO) method[63,64] at the B3LYP/BS2//B3LYP/BS1 level. Prior to these calculations, for H$_2$Salen, we performed B3LYP/BS2//B3LYP/BS1, B3LYP/BS3//B3LYP/BS1, and corresponding B3LYP/BS2//B3LYP/BS2 and B3LYP/BS3//B3LYP/BS3 calculations to test the reliability of the chosen

---

(47) Imagawa, K.; Nagata, T.; Yamada, T.; Mukaiyama, T. *Chem. Lett.* **1994**, 527−530. Mukaiyama, T.; Yamada, T. *Bull. Chem. Soc. Jpn.* **1995**, *68*, 8, 17−35.

(48) Collman, J. P.; Chien, A. S.; Eberspacher, T. A.; Zhong, M.; Brauman, J. I. *Inorg. Chem.* **2000**, *39*, 4625−4629.

(49) Frisch, M. J.; Trucks, G. W.; Schlegel, H. B.; Scuseria, G. E.; Robb, M. A.; Cheeseman, J. R.; Zakrzewski, V. G.; Montgomery, J. A., Jr.; Stratmann, R. E.; Burant, J. C.; Dapprich, S.; Millam, J. M.; Daniels, A. D.; Kudin, K. N.; Strain, M. C.; Farkas, O.; Tomasi, J.; Barone, V.; Cossi, M.; Cammi, R.; Mennucci, B.; Pomelli, C.; Adamo, C.; Clifford, S.; Ochterski, J.; Petersson, G. A.; Ayala, P. Y.; Cui, Q.; Morokuma, K.; Malick, D. K.; Rabuck, A. D.; Raghavachari, K.; Foresman, J. B.; Cioslowski, J.; Ortiz, J. V.; Stefanov, B. B.; Liu, G.; Liashenko, A.; Piskorz, P.; Komaromi, I.; Gomperts, R.; Martin, R. L.; Fox, D. J.; Keith, T.; Al-Laham, M. A.; Peng, C. Y.; Nanayakkara, A.; Gonzalez, C.; Challacombe, M.; Gill, P. M. W.; Johnson, B. G.; Chen, W.; Wong, M. W.; Andres, J. L.; Head-Gordon, M.; Replogle, E. S.; Pople, J. A. *Gaussian 98*, revision A.6; Gaussian, Inc.: Pittsburgh, PA, 1998.

(50) Becke, A. D. *Phys. Rev. A: At., Mol., Opt. Phys.* **1988**, *38*, 3098−3100.

(51) Becke, A. D. *J. Chem. Phys.* **1993**, *98*, 5648−5652.

(52) Lee, C.; Yang, W.; Parr, R. G. *Phys. Rev. B: Condens. MatterMater. Phys.* **1988**, *37*, 785.

(53) Perdew, J. P. *Phys. Rev. B: Condens. Matter Mater. Phys.* **1986**, *33*, 8822−8824.

(54) Roothaan, C. C. J. *Rev. Mod. Phys.* **1951**, *23*, 69−89. Pople, J. A.; Nesbet, R. K. *J. Chem. Phys.* **1954**, *22*, 571−574.

(55) Dunning, T. H.; Hay, P. J. In *Modern Theoretical Chemistry*; Schaefer, H. F., III, Ed.; Plenum: New York, 1977; Vol. 3, pp 1−27.

(56) Hay, P. J.; Wadt, W. R. *J. Chem. Phys.* **1985**, *85*, 299−310. Hay, P. J.; Wadt, W. R. *J. Chem. Phys.* **1985**, *82*, 270−283.

(57) Wadt, W. R.; Hay, P. J. *J. Chem. Phys.* **1985**, *82*, 284−298.

(58) Dolg, M.; Wedig, U.; Stoll, H.; Preuss, H. *J. Chem. Phys.* **1987**, *82*, 866−872.

(59) Igel-Mann, G.; Stoll, H.; Preuss, H. *Mol. Phys.* **1988**, *65*, 1321−1328.

(60) Krishnan, R.; Binkley, J. S.; Seeger, R.; Pople, J. A. *J. Chem. Phys.* **1980**, *72*, 650−654.

(61) Schaftenaar, G.; Noordik, J. H. *J. Comput.-Aided Mol. Design* **2000**, *14*, 123−134.

(62) Flükiger, P.; Lüthi, H. P.; Portmann, S.; Weber, J. *MOLEKEL, 4.0*; Swiss Center for Scientific Computing: Manno, Switzerland, 2000.

(63) Pulay, P.; Wolinski, K.; Hinton, J. F. *NATO ASI Ser., Ser. C* **1993**, *386*, 243−262.

(64) Cheeseman, J. R.; Trucks, G. W.; Keith, T. A.; Frisch, M. J. *J. Chem. Phys.* **1996**, *104*, 5497−5509.

Table 2. Relative Energies (kcal/mol) of Different Isomers and Transition States of Species **1**−**3** Calculated with the B3LYP Functional with Different Basis Sets

species	state	BS1//BS1	BS2//BS1	species	state	BS1//BS1	BS2//BS1
1-oxo	^{1}A	2.1	1.0	**TS-1-N-oxo_a**	^{5}A	20.4	21.7
	^{3}A	0.0	0.0	**TS-1-N-oxo_b**	^{5}A	19.5	21.0
	^{5}A	1.2	2.0	**1-Imd-N-oxo_a**	^{5}A	−9.0	−16.4
1-Imd-oxo	^{1}A-R	16.7	13.2	**1-Imd-N-oxo_b**	^{5}A	−3.2	−12.0
	^{1}A-U	14.4	12.3	**2-Imd-N-oxo_a**	^{4}A	32.0	27.9
	^{3}A	0.4	0.3	**2-Imd-N-oxo_b**	^{4}A	30.5	28.0
	^{5}A	0.0	0.0	**TS-1-Imd-N-oxo_a**	^{5}A	21.2	20.3
2-oxo	^{2}A	6.7	6.4	**TS-1-Imd-N-oxo_b**	^{5}A	21.5	20.6
	^{4}A	0.0	0.0	**1-peroxo_a**	^{5}A	14.7	13.8
2-Imd-oxo	^{2}A	11.8	11.5		^{3}A	41.5	
	^{4}A	0.0	0.0	**1-peroxo_b**	^{5}A	17.0	16.0
1-N-oxo_a	^{5}A	−4.0	−9.8		^{3}A		
	^{3}A	16.7	14.8	**2-peroxo_a**	^{4}A	49.1	50.8
1-N-oxo_b	^{5}A	−6.2	−11.5		^{2}A	70.0	
	^{3}A	18.6	15.2	**2-peroxo_b**	^{4}A	51.4	52.8
2-N-oxo_a	^{4}A	33.8	30.0		^{2}A	72.1	
	^{2}A	52.9		**3**	^{1}A	0.0	0.0
2-N-oxo_b	^{4}A	28.6	25.8		^{3}A	19.6	21.7
	^{2}A	50.7			^{5}A	33.1	39.0

approximation. In these calculations, we used tetramethylsilane $Si(CH_3)_4$ (TMS), ammonia (NH_3), and methanol (CH_3OH) as a reference for ^{1}H and ^{13}C, ^{15}N, and ^{17}O chemical shift calculations, respectively.

III. Results and Discussion

This section is organized as follows. In subsection A, we discuss the electronic and geometric structures of the complexes [L(Salen)Mn(V)O]$^+$ (**1-oxo**) and [L(Salen)Mn(IV)O] (**2-oxo**), their **N-oxo** and **peroxo** isomers, [L(OSalen)-Mn(III)]$^+$ and [L(OSalen)Mn(II)], respectively, and then complex [(Salen)Mn(V)N] (**3**), with L = Imd and none. Section B is devoted to the discussion of the calculated NMR chemical shift data.

In our discussions, we use B3LYP/BS2//B3LYP/BS1 energies, unless otherwise indicated. In Table 1, we compare the relative energies of **1-oxo** species calculated at different levels of theory, while in Table 2, we present calculated relative energies at the B3LYP level for all species in the present study. Table 3 summarizes important calculated geometrical parameters for all species. In Figure 1, molecular orbital diagrams of the calculated species are presented. Figure 2 presents calculated structures of intermediates and transition states for complexes **1**. Since obtained structures for species **2-oxo** and **3** are very similar to those of **1-oxo**, we only present their important geometrical parameters in Table 3. Tables 4−6 present the calculated ^{1}H, ^{13}C, and ^{15}N and ^{17}O NMR chemical shifts, respectively, with the atomic labels shown in Scheme 3. The Supporting Information contains six tables. Tables S1, S2, and S3 present distances of Mn and the terminal X atom from selected molecular planes, calculated atomic spin densities, and Mulliken charges, respectively. Table S4 includes the geometries of H_2Salen calculated at different levels of theory. We also included Cartesian coordinates of all calculated species in Table S5 and their total, zero-point corrected, and Gibbs free energies in Table S6.

A. Geometries, Electronic Structures, and Energies of Species 1−3. Cationic Oxo Complex, [(Salen)Mn(V)O]$^+$ (1-Oxo). As seen in Table 2, at the B3LYP level the triplet ^{3}A state is found to be the ground state for the complex **1-oxo** species. Its singlet ^{1}A and quintet ^{5}A states lie 1.0 and 2.0 kcal/mol higher, respectively**.** Since the energy gaps among the three low-lying states are small, we conclude that all three spin states should be considered for proper description of the reactivity of **1-oxo**.

Because of possible flaws of the B3LYP functional predicting the energetics, for this particular system (see Introduction), we have systematically compared results of three other density functionals (BLYP, BP86, and B3P86), as well as HF, with the same basis sets. As seen in Table 1, both hybrid functionals, B3LYP and B3P86, agree within 1−3 kcal/mol on the relative order of the spin states (^{3}A < ^{1}A < ^{5}A) predicting triplet to be the ground state, whereas both nonhybrid functionals, BLYP and BP86, also agree between themselves in the state ordering (^{1}A < ^{3}A ≪ ^{5}A) within 1−2 kcal/mol but favor the singlet state.

Thus, comparison of hybrid functionals with pure functionals shows that the latter destabilize high-spin states. Table 1 shows that the origin of such discrepancy lies in the HF contribution. At the HF level, the ordering of states is significantly different from any of the above (^{3}A < ^{5}A ≪ ^{1}A). In other words, the HF method strongly favors high-spin states and, consequently, lowers high-spin states at the hybrid density functional levels, such as B3LYP and B3P86. The same observation was made earlier for some Fe complexes and, therefore, appears to be general.[65] Although, the accuracy of hybrid DFT methods in describing relative energies of low-lying electronic states in general constitutes a question, we find that B3LYP performs satisfactorily well for the systems under investigation. Specifically, the B3LYP method predicts the correct ground state for the species **2-oxo**, **3**, and parent [(Salen)Mn(III)]$^+$ complex (see later description). Furthermore, description of the relative energies of low-lying electronic states is not main purpose of this paper. Therefore, throughout this work we have used the B3LYP method. Also, we suggest that future studies of

---

(65) Reiher, M.; Salomon, O.; Hess, B. A. *Theor. Chem. Acc.* **2001**, *107*, 48−55.

Table 3. Calculated Important Geometrical Parameters (Distances in Å and Angles in deg) of Species **1**−**3**

species	state	Mn−O^1	Mn−O^2	Mn−N^1	Mn−N^2	Mn−X^3	R$_1$[a]	R$_2$[a]	R$_3$[a]	D$_1$[a]
1-oxo	^{1}A	1.82	1.85	1.95	1.93	1.55	2.69	2.81		
	^{3}A	1.79	1.83	2.00	1.96	1.62	2.66	2.74		
	^{5}A	1.86	1.87	1.96	1.98	1.68	2.61	2.70		
1-Imd-oxo	^{1}A−R	1.85	1.86	1.96	1.97	1.56	2.57	2.60	2.30	24
	^{1}A−U	1.84	1.86	1.99	1.98	1.60	2.60	2.58	2.24	16
	^{3}A	1.84	1.86	2.00	1.99	1.78	2.66	2.55	2.11	11
	^{5}A	1.88	1.87	1.99	1.98	1.75	2.56	2.62	2.11	16
2-oxo	^{2}A	1.86	1.92	2.00	1.94	1.60	2.62	2.82		
	^{4}A	1.88	1.87	1.99	2.00	1.66	2.65	2.68		
2-Imd-oxo	^{2}A	1.93	1.96	1.97	1.98	1.62	2.62	2.63	2.27	20
	^{4}A	1.92	1.92	2.00	2.00	1.68	2.62	2.61	2.24	13
1-N-oxo_a	^{5}A	1.87	1.83	2.66	2.02	1.87	1.40	2.80		
	^{3}A	1.81	1.78	2.70	1.96	1.88	1.41	2.79		
1-N-oxo_b	^{5}A	1.83	1.86	2.00	2.59	1.90	2.71	1.41		
	^{3}A	1.81	1.82	1.98	2.62	1.91	2.72	1.41		
2-N-oxo_a	^{4}A	1.92	1.86	2.60	1.97	1.93	1.40	2.81		
	^{2}A	1.93	1.88	2.69	1.97	1.99	1.39	2.92		
2-N-oxo_b	A	1.86	1.89	1.97	2.44	1.94	2.73	1.42		
	^{2}A	1.87	1.91	1.96	2.62	1.99	2.74	1.39		
TS-1-N-oxo_a	^{5}A	1.88	1.82	2.00	1.97	1.87	1.81	2.89		
TS-1-N-oxo_b	^{5}A	1.82	1.88	1.97	1.99	1.86	2.75	1.85		
1-Imd-N-oxo_a	^{5}A	1.88	1.85	2.83	2.22	1.97	1.40	2.77	2.04	2
1-Imd-N-oxo_b	^{5}A	1.88	1.89	2.00	2.57	1.94	2.65	1.40	2.23	28
2-Imd-N-oxo_a	^{4}A	1.97	1.94	2.83	2.21	2.02	1.39	2.83	2.05	−7.5
2-Imd-N-oxo_b	^{4}A	1.96	1.86	2.01	2.26	1.92	2.69	1.46	2.27	18
TS-1-Imd-N-oxo_a	^{5}A	1.87	1.89	2.03	1.99	1.88	1.74	2.66	2.10	6
TS-1-Imd-N-oxo_b	^{5}A	1.87	1.88	1.99	2.01	1.89	2.64	1.74	2.12	22
1-peroxo_a	^{5}A	2.38	1.83	2.03	1.99	1.87	1.54	2.73		
	^{3}A	2.27	1.82	2.02	1.99	1.86	1.54	2.74		
1-peroxo_b	^{5}A	1.83	2.50	1.98	2.03	1.85	2.74	1.53		
2-peroxo_a	^{4}A	2.55	1.87	1.99	1.97	1.89	1.53	2.77		
	A	2.55	1.89	2.02	1.98	1.88	1.55	2.77		
2-peroxo_b	A	1.87	2.68	1.97	1.99	1.88	2.74	1.52		
	^{2}A	1.90	2.79	1.98	2.04	1.83	2.70	1.56		
3	^{1}A	1.91	1.92	1.97	1.97	1.51	2.70	2.77		
	^{3}A	1.88	1.88	2.00	1.98	1.64	2.66	2.73		
	^{5}A	1.87	1.86	1.96	1.96	1.86	2.66	2.75		
exptl (**3**)	^{1}A[b]	1.90	1.92	1.95	1.95	1.51	2.68	2.70		

[a] R$_1$ = X^3−O^1 for **peroxo** species and X^3−N^1 for the rest; R$_2$ = X^3−O^2 for **peroxo** species and X^3−N^2 for the rest; R$_3$ = Mn−N^4; D$_1$ = O^2−Mn−N^4−C, where the carbon atom in the dihedral refers to C^2 carbon atom of Imd. [b] Refs 11 and 71.

reactivity of the oxo species must address all low-lying spin states, since neither hybrid nor pure density functionals provide ultimate answer.

It is worth noting that both Linde et al.[40] and Strassner et al.[41] used B3LYP with all-electron basis sets and obtained different ordering of states for the same **model_I** (X = O, L = none): ^{3}A < ^{1}A < ^{5}A and ^{1}A < ^{3}A ≪ ^{5}A, respectively. The latter is similar to that obtained by Abashkin et al.[46] at the BP86 level. Furthermore, Plattner et al.[22,42] also predicted the ordering ^{1}A < ^{3}A ≪ ^{5}A (see Table 1) for **model_II** (X = O, L = none) using the B3LYP method with all electron basis set.

In order to describe the nature of these three spin states, we have analyzed their molecular orbitals calculated as described in section II. Figure 1A schematically represents the MO interaction diagram for formation of **1-oxo** species from Salen, oxygen (O^3), and Mn ion. The Mn d-orbitals split in the square pyramidal environment into three groups ($d_{x^2-y^2}$, d_{xz}, and d_{yz}; d_{z^2}; and d_{xy}) and interact with the p-orbitals of terminal O^3 and S$_{\mathrm{SALC}}$ orbital of Salen (symmetry-adapted linear combination composed mainly of $p_{x,y}$ orbitals of two basal Salen oxygen atoms O^1 and O^2). These interactions result in five doubly occupied orbitals, $\sigma(d_{z^2} + p_z(O^3))$, $\pi(d_{xz} + p_x(O^3))$, $\pi(d_{yz} + p_y(O^3))$, $\delta(d_{x^2-y^2} + S_{SALC})$, and $\delta(d_{x^2-y^2} - S_{SALC})$ for the singlet state of **1-oxo**. The low-lying virtual orbitals are antibonding $\pi^*(d_{xz} - p_x(O^3))$, $\pi^*(d_{yz} - p_y(O^3))$, and $\sigma^*(d_{z^2} - p_z(O^3))$ orbitals. The d_{xy}-orbital is a nonbonding orbital.

According to this interaction diagram, the singlet state ^{1}A has $[\sigma(d_{z^2} + p_z(O^3))]^2[\pi(d_{xz} + p_x(O^3))]^2[\pi(d_{yz} + p_y(O^3))]^2[\delta(d_{x^2-y^2} + S_{SALC})]^2[\delta(d_{x^2-y^2} - S_{SALC})]^2$ electron configuration. Corresponding triplet state ^{3}A with $[\sigma(d_{z^2} + p_z(O^3))]^2[\pi(d_{xz} + p_x(O^3))]^2[\pi(d_{yz} + p_y(O^3))]^2[\delta(d_{x^2-y^2} + S_{SALC})]^2[\delta(d_{x^2-y^2} - S_{SALC})]^1[\pi^*(d_{xz} - p_x(O^3))]^1$ electron configuration arises from promotion of one electron from the doubly occupied $\delta(d_{x^2-y^2} - S_{SALC})$ orbital into the antibonding π^*-orbital of the Mn−O^3 bond, while the quintet state ^{5}A with the $[\sigma(d_{z^2} + p_z(O^3))]^2[\pi(d_{xz} + p_x(O^3))]^2[\pi(d_{yz} + p_y(O^3))]^2[\delta(d_{x^2-y^2} + S_{SALC})]^1[\delta(d_{x^2-y^2} - S_{SALC})]^1[\pi^*(d_{xz} - p_x(O^3))]^1[\pi^*(d_{yz} - p_y(O^3))]^1$ electron configuration is obtained by further promotion of an electron from the second $\delta(d_{x^2-y^2} + S_{SALC})$ orbital to the other antibonding π^*-orbital of the Mn−O^3 bond (Figure 1B).

On the basis of the electron configurations discussed already, we may expect that the formal bond order of the Mn−O^3 terminal bond will decrease from 3 to $^5/_2$ and 2 going from ^{1}A to ^{3}A and ^{5}A states. These formal bond orders are consistent with the computed Mn−O^3 bond lengths given

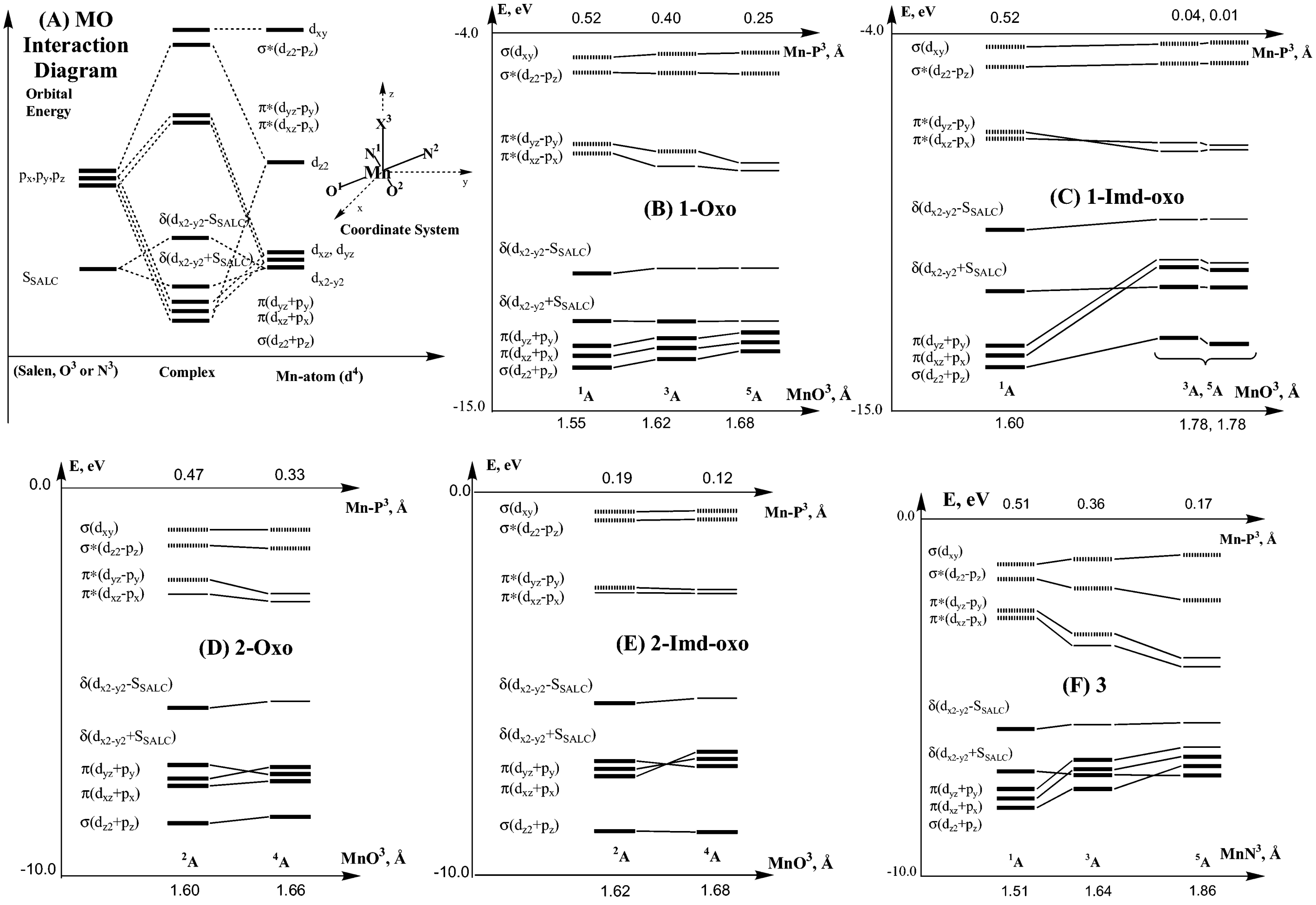

Figure 1. (A) Qualitative MO interaction diagram between Salen, O^3 or N^3, and Mn(III, d^4). Also shown is the coordinate system used here. (B−F) The MO diagrams of different spin states of the species **1-oxo**, **1-Imd-oxo**, **2-oxo**, **2-Imd-oxo**, and **3**, respectively, indicating changes in individual MO energies upon changes in geometries.

in Table 3; calculated Mn−O^3 bond length increases in the order ^{1}A (1.55 Å) < ^{3}A (1.62 Å) < ^{5}A (1.68 Å). However, the obtained trend, ^{1}A (1033 cm^{-1}) > ^{5}A (785 cm^{-1}) > ^{3}A (625 and 697 cm^{-1}), in the calculated Mn−O^3 vibrational frequencies, is not consistent with the trend in the Mn−O^3 bond distance already reported. This could be rationalized by analyzing the nature of the Mn−O^3 normal vibrational frequencies. Indeed, in ^{1}A, this frequency is a pure Mn−O^3 stretching, while the two vibrations in the ^{3}A are coupled with the stretching of the two basal Mn−O^1 and Mn−O^2 bonds. The vibration for the quintet state also is mainly Mn−O^3 stretching, while it is slightly coupled with the bending of the O^1−Mn−O^2 angle. Perhaps, for correct comparison of the bond strengths in different spin states with their vibrational frequencies, one needs to uncouple the Mn−O^3 motions from the other motions, which could be done with the adiabatic internal motions (AIM) vibrational analysis[66] but is not the subject of the present paper.

Another significant geometrical change in the complex **1-oxo** upon changing its electronic state is the displacement of the Mn atom from the mean basal ligand plane, Mn−P^3 distance (see Table 1S), which decreases in the order ^{1}A (0.52 Å) > ^{3}A (0.40 Å) > ^{5}A (0.25 Å). This motion correlates with the changes in the Mn−O^3 bond distance discussed already. Therefore, one may conclude that an increase in the multiplicity of **1-oxo** elongates the terminal Mn−O^3 bond distance and reduces the displacement of the Mn atom from the mean basal plane.

Changes in other geometrical parameters of **1-oxo** upon changing its spin state are not significant and do not follow a simple trend. Therefore, we will not discuss these changes in more detail; instead, we provide Cartesian coordinates of all calculated species in the Supporting Information (Table S5).

Cationic Oxo Complex with Imd Axial Ligand, [Imd-(Salen)Mn(V)O]$^+$ (1-Imd-oxo). Calculations for ^{1}A, ^{3}A, and ^{5}A spin states of the complex **1-Imd-oxo**, with an axial imidazole ligand, show that its high-spin state ^{5}A is a pure quintet state with $\langle S^2\rangle = 6.06$, while open shell singlet and triplet states are heavily spin-contaminated, with $\langle S^2\rangle$ of 0.87 and 2.96, respectively. Therefore, one may expect to obtain reliable geometry and energy parameters only for the high-spin state, ^{5}A, at the conventional B3LYP level. Calculation of the reliable geometry and energy parameters for the ^{1}A and ^{3}A states would need a multireference based method, such as CASSCF and MCSCF, or a special approach with a

---

(66) Konkoli, Z.; Cremer, D. *Int. J. Quantum Chem.* **1998**, *67*, 1−9. Konkoli, Z.; Larsson, J. A.; Cremer, D. *Int. J. Quantum Chem.* **1998**, *67*, 11−27. Konkoli, Z.; Cremer, D. *Int. J. Quantum Chem.* **1998**, *67*, 29−40. Konkoli, Z.; Larsson, J. A.; Cremer, D. *Int. J. Quantum Chem.* **1998**, *67*, 41−55.

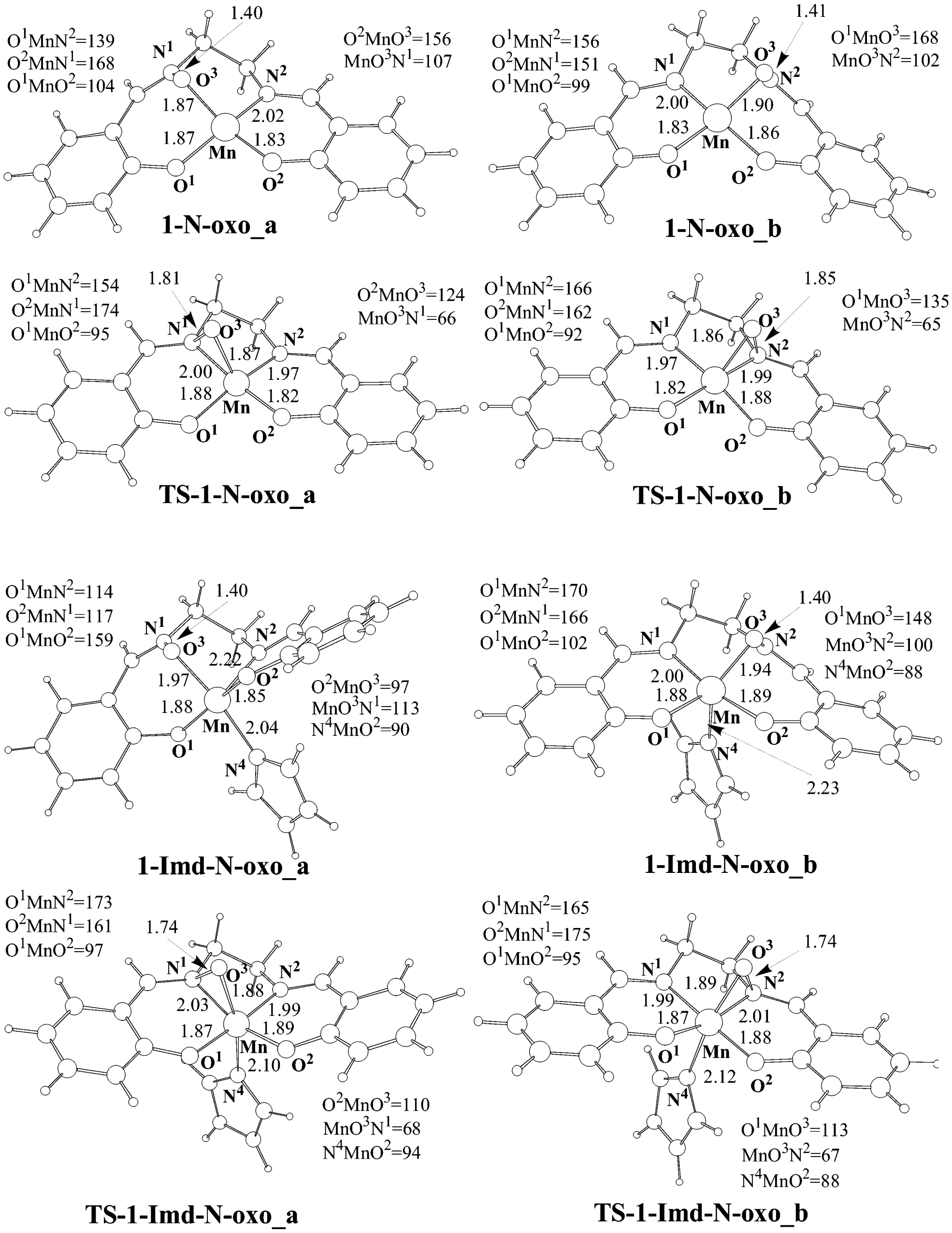

Figure 2. Calculated geometries (distances in Å and angles in deg) of **1-N-oxo** and **1-Imd-N-oxo** species and the corresponding **TS-1-N-oxo** and **TS-1-Imd-N-oxo** transition states.

Scheme 3. Atomic Labels Used in NMR Chemical Shift Discussions[a]

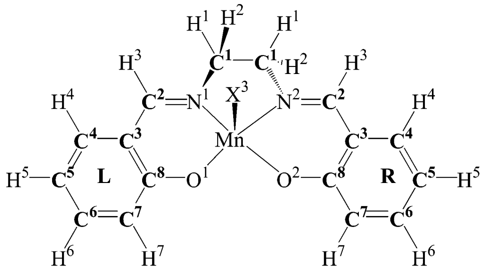

[a] H^8 in the text refers to the OH protons of H$_2$Salen not shown in this scheme.

symmetry broken solution.[67,68] Multireference methods are technically impractical for such a large system as **1-oxo**. Therefore, here we use the symmetry broken approach of Yamaguchi[67] to obtain an estimate of the energy of the pure low-spin states of **1-Imd-oxo** from spin-contaminated calculations. The geometries of the singlet and triplet states of these complexes have been optimized at the conventional B3LYP level. For the singlet state, we have performed two different calculations using restricted and unrestricted B3LYP methods, called ^{1}A-R and ^{1}A-U, respectively. The results given in Table 3 show that the UB3LYP method provides a somewhat longer Mn$-$O^3 bond length (1.60 Å) compared to that from RB3LYP (1.56 Å). Attempts to obtain the geometry of the triplet ^{3}A state by UB3LYP have led to a number of solutions, and in Tables 2 and 3, we present results

---

(67) Yamaguchi, K.; Fukui, H.; Fueno, T. *Chem. Lett.* **1986**, 625$-$628. Yamaguchi, K. *Chem. Phys. Lett.* **1988**, *149*, 537$-$542.

(68) Noodleman, L.; Norman, J. G., Jr. *J. Chem. Phys.* **1979**, *70*, 4903$-$4906. Noodleman, L. *J. Chem. Phys.* **1981**, *74*, 5737$-$5743.

only for the lowest triplet state, which has a geometry similar to those of the ^{5}A state with the Mn$-$O^3 bond length of 1.78 Å.

As seen in Table 2, the relative energies for the different spin states of the **1-oxo** complex are altered in the presence of the axial imidazole ligand. For complex **1-Imd-oxo**, ^{5}A has the lowest energy, followed by ^{3}A, which is 0.3 kcal/mol higher. The singlet state ^{1}A-U and ^{1}A-R are energetically highly (>12 kcal/mol) unfavorable.

As noted already, since low-spin state solutions tend to be highly spin contaminated, we applied the Yamaguchi correction scheme[67] with BS1 to obtain correction to the energies.[67] In brief, the Yamaguchi correction scheme is based on the assumption that exchange coupling between two localized spins in molecular systems can be described by the Heisenberg Hamiltonian:

$$\hat{H} = -2\sum_{a>b} J_{ab}\vec{S}_a\cdot\vec{S}_b$$

where J_{ab} is the effective exchange integral for the radical sites with the spin operators $\vec{S}_a$ and $\vec{S}_b$. It can be computed within the ab initio (or/and DFT) spin-projected unrestricted Hartree$-$Fock (PUHF) approximation via the formula

$$J_{ab} \cong \frac{{}^{\mathrm{LS}}E(\mathrm{UHF}) - {}^{\mathrm{HS}}E(\mathrm{UHF})}{{}^{\mathrm{HS}}\langle \mathbf{S}^2\rangle(\mathrm{PUHF}) - {}^{\mathrm{LS}}\langle \mathbf{S}^2\rangle(\mathrm{UHF})}$$

On the basis of the J_{ab} value, it is possible to correct the UHF energy of the low-spin (LS) state:

$${}^{\mathrm{LS}}E(\mathrm{PUHF}) = {}^{\mathrm{LS}}E(\mathrm{UHF}) + J_{ab}[{}^{\mathrm{LS}}\langle \mathbf{S}_2\rangle(\mathrm{UHF}) - m(m+1)]$$

where m is the half of the number of α electrons minus the number of β electrons. Thus, to correct the energies of spin-contaminated low-spin complexes, one would need to compute high-spin energies at the low-spin geometries. In our calculations, we use the UB3LYP method instead of UHF in the given formula.

Applying the Yamaguchi correction to ^{1}A-U and ^{3}A states of **1-Imd-oxo** only slightly changes the energies of the ^{1}A and ^{3}A states; it destabilizes the singlet by 0.4 kcal/mol but stabilizes ^{3}A by 0.3 kcal/mol, relative to uncorrected solutions, respectively.

Our detailed MO analysis (not shown here for brevity) indicates that the imidazole ligand interacts with **1-oxo** almost exclusively through the d_{z^2} orbital on Mn. This in turn significantly destabilizes $\delta(d_{x^2-y^2} + S_{\mathrm{SALC}})$ and $\delta(d_{x^2-y^2} - S_{\mathrm{SALC}})$ orbitals and, in addition, destabilizes bonding π- and σ-orbitals in the ^{3}A and ^{5}A states. As a result, the MO picture for **1-Imd-oxo** (Figure 1C) changes qualitatively from that for **1-oxo**. Interestingly, the triplet and quintet states of **1-Imd-oxo** both have 4 unpaired electrons and are similar in MOs and geometry.

Neutral Complex, [(Salen)Mn(IV)O] (2-Oxo). The neutral complex, **2-oxo**, which differs from the cationic **1-oxo** by one extra electron, may have two low-lying electronic states, ^{2}A and ^{4}A, with electronic configurations of $[\sigma(d_{z^2} + p_z(O^3))]^2[\pi(d_{xz} + p_x(O^3))]^2[\pi(d_{yz} + p_y(O^3))]^2[\delta(d_{x^2-y^2} + S_{\mathrm{SALC}})]^2[\delta(d_{x^2-y^2} - S_{\mathrm{SALC}})]^2[\pi^*(d_{xz} - p_x(O^3))]^1$ and $[\sigma(d_{z^2} + p_z(O^3))]^2[\pi(d_{xz} + p_x(O^3))]^2[\delta(d_{x^2-y^2} + S_{\mathrm{SALC}})]^2[\pi(d_{yz} + p_y(O^3))]^2[\delta(d_{x^2-y^2} - S_{\mathrm{SALC}})]^1[\pi^*(d_{xz} - p_x(O^3))]^1[\pi^*(d_{yz} - p_y(O^3))]^1$, respectively (see Figure 1D). As seen in Table 1, the quartet ^{4}A state is found to be the ground state, while the doublet lies 6.4 kcal/mol higher in energy.

As in the case with cationic oxo-species, geometry of the neutral oxo-species also depends on the electronic state. As seen from Table 3 and Table 1S, in the neutral complex **2-oxo**, the Mn$-$O^3 bond length increases from 1.60 to 1.66 Å, while Mn$-$P^3 decreases from 0.47 to 0.33 Å, going from ^{2}A to ^{4}A. In other words, trends in geometry change for **2-oxo** accompanying the spin state change are similar to those of **1-oxo**, discussed already. Comparison of calculated Mn-O^3 bond lengths in the ^{2}A and ^{4}A states of 2-oxo with those of ^{1}A and ^{3}A states of **1-oxo**, respectively, shows that addition of one electron to the antibonding π*-orbital elongates the Mn$-$O^3 bond length by 0.04$-$0.05 Å. As already discussed, similar effects were found for **1-oxo** upon promotion of one electron from doubly occupied δ-orbitals to empty π*-orbitals.

As seen from the MO correlation diagram (see Figure 1D), the formal bond order of the ^{2}A and ^{4}A states of **2-oxo** is identical to that of the ^{3}A and ^{5}A states of **1-oxo**, respectively. The calculated harmonic Mn$-$O^3 bond stretching frequencies for the low-lying electronic states **2-oxo** show the following trend: ^{2}A(964 cm^{-1}) > ^{4}A(874 and 877 cm^{-1}).

Neutral Complex, [Imd(Salen)Mn(IV)O] (2-Imd-oxo). As in the case with **1-Imd-oxo**, the solution for the low-spin state of **2-Imd-oxo**, ^{2}A, is highly spin contaminated with $\langle S^2\rangle = 1.28$, while its high-spin state, ^{4}A, is nearly a pure spin state with $\langle S^2\rangle = 3.81$. Therefore, once again, one may expect more reliable B3LYP results for the high-spin state, ^{4}A. As seen in Table 2, the ^{2}A state lies 11.5 kcal/mol higher than ^{4}A in **2-Imd-oxo**, which is 5 kcal/mol larger than the corresponding value in **2-oxo**. Thus, the coordination of the imidazole ligand destabilizes the low-spin state of the complex. It is noteworthy that the inclusion of the Yamaguchi correction increases the ^{2}A$-$^{4}A energy gap by 1.9 kcal/mol.

As seen in Figure 1E, the effect of the imidazole ligand on the MO picture is modest. The only difference is observed in the ^{4}A state where the lower of the two δ orbitals descends below the two π orbitals. However, this does not affect the formal bond order since the referred orbitals are doubly occupied. The effect of the imidazole on the geometries is straightforward; interaction of imidazole with Mn causes the elongation of the Mn$-$O^3 bond by 0.02 Å compared to that of **2-oxo**, in both ^{2}A and ^{4}A states. Imidazole also decreases the degree of Mn displacement from the basal plane from 0.47 to 0.19 Å and from 0.33 to 0.12 Å for ^{2}A and ^{4}A, respectively.

Finally, we have computed the adiabatic ionization potential (IP) of the neutral oxo species **2-oxo** as IP = E_{tot}(**2-oxo (^{4}A)**) $-$ E_{tot}(**1-oxo (^{3}A)**) and **2-Imd-oxo** as IP$_{\mathrm{Im}}$ = E_{tot}(**2-Imd-oxo (^{4}A)**) $-$ E_{tot}(**1-Imd-oxo (^{5}A)**) and have found it to be 6.99 and 6.42 eV, respectively. Therefore, the axial imidazole ligand reduces the IP of the system.

N-oxo and Peroxo Isomers of Species 1 and 2. In preceding paragraphs, we discussed electronic and geometrical structures of the species **1-oxo** and **2-oxo**, where the O^3-ligand is located in the axial position. However, those species may have other isomers, $[(OSalen)Mn(III)]^+$, **1-N-oxo**, and [(OSalen)Mn(II)], **2-N-oxo**, and $[(OSalen)Mn(III)]^+$, **1-peroxo**, and [(OSalen)Mn(II)], **2-peroxo**, corresponding to insertion of the O^3-ligand into Mn−N(Salen) and Mn−O(Salen) bonds, respectively. To our best knowledge, these isomers of species **1-oxo** and **2-oxo** have never been discussed in the literature for the Salen derived Mn complexes. It is worth noting, however, that the species analogous to **1-N-oxo** has been predicted to exist for Mn−porphyrin complexes[29] and tentatively has been structurally characterized.[30] In this part of the paper, we discuss electronic and geometrical structures, as well as relative stabilities of these **N-oxo** and **peroxo** isomers.

$[(OSalen)Mn(III)]^+$ (1-N-oxo) and [(OSalen)Mn(II)] (2-N-oxo) Species. In general, **N-oxo** isomers may have two distinct forms corresponding to the position of the O^3-ligand relative to the two carbon atoms of the puckered (twisted) diimine bridge, where one of the carbon atoms of the bridge is located above (C^a), while the other is located below (C^b), the N^1−Mn−N^2 plane. If insertion of the O^3-ligand into the Mn−N bond occurs on the C^a side, then the isomer is labeled as **a**. On the other hand, if insertion occurs on the C^b side, the isomer is labeled as **b**. Thus, in this notation, for the cationic and neutral **N-oxo** species we may have **1-N-oxo_a**, **1-N-oxo_b**, and **2-N-oxo_a**, **2-N-oxo_b** isomers, respectively (Scheme 1).

As seen in Table 2, the ground electronic states of the isomers **1-N-oxo_a** and **1-N-oxo_b** are quintet states ^5A, with the triplet ^3A states lying 24.6 and 26.8 kcal/mol higher, respectively. Similarly, the isomers **2-N-oxo_a** and **2-N-oxo_b** of neutral species **2** have a ground ^4A state, and their doublet ^2A states lie about 19.1 and 22.1 kcal/mol higher (at the B3LYP/BS1 level). In other words, the calculated high-spin states of the **N-oxo** isomers of both neutral and cationic species lie about 19−27 kcal/mol lower than corresponding low-spin states. At their ground high-spin states, the isomer **N-oxo_b** is found to be lower than isomer **N-oxo_a** by 1.7 and 4.3 kcal/mol for **1-N-oxo** and **2-N-oxo**, respectively.

However, the most intriguing finding is that the isomers **1-N-oxo_a** and **1-N-oxo_b** at their lowest ^5A states lie 9.8 and 11.5 kcal/mol lower than the **1-oxo** species in its lowest ^3A state and are separated from the latter by significant, 21.7 and 21.0 kcal/mol, energy barriers, respectively. The transition states, **TS-1-N-oxo_a** and **TS-1-N-oxo_b**, corresponding to these barriers, are represented in Figure 2 and are found to have one imaginary frequency, 607i and 592i cm^{-1}, respectively. Thus, these results clearly indicate that, in species **1-oxo**, the insertion of the terminal O^3-ligand into the basal Mn−N bonds is thermodynamically favorable and could occur with moderate energetic barriers.

Since the **1-N-oxo** species in their ^5A ground state demonstrate outstanding stability relative to **1-oxo** species, we feel that it is necessary to describe geometrical parameters of **1-N-oxo** species in more detail here (see Figure 2). Note that a similar **N-oxo** species has been experimentally identified for Ni,[26] Fe,[14,27] and, tentatively, Mn[30] porphyrins.

Starting from the ^5A **1-oxo** species, one has to go through the **TS-1-N-oxo_a** transition state to form the **1-N-oxo_a** product. As seen in Figure 2, this transition state has a characteristic triangular arrangement of ligands O^3 and N^1 and Mn. Such an arrangement causes the Mn−O^3 bond to elongate from 1.68 to 1.87 Å, and the basal bond Mn−N^1 to elongate from 1.96 to 2.00 Å, while its trans counterpart Mn−O^2 shrinks from 1.87 to 1.82 Å compared to the bonds in parent **1-oxo**. The new bond O^3−N^1 is being formed reaching 1.81 Å at **TS-1-N-oxo_a**. In the product **1-N-oxo_a**, the triangle is broken leaving the Mn−O^3 bond at 1.87 Å and rendering Mn−N^1 and Mn−O^2 to 2.66 and 1.83 Å, respectively. The bond O^3−N^1 is now formed and is 1.40 Å. It is worth noting that the Mn−O^3 bond length of 1.87 Å is extremely close to an unidentified Mn−O bond of 1.84 Å in the EXAFS/XANES study of Mn−porphyrin with NaOCl,[30] and also the theoretically predicted value of 1.84 Å in the Mn−N-oxo porphyrin complex.[29] Similar trends were observed for transition state **TS-1-N-oxo_b** and product **1-N-oxo_b**, which will not be repeated here.

Since the interaction between Mn and O^3 in the **N-oxo** species is not covalent in nature, and also, the obtained canonical orbitals are highly deformed from conventional square pyramidal d-orbitals, we characterized their electronic states only by spin density (Table 2S). We find that the four unpaired electrons are localized entirely on the Mn atom, which corresponds to the Mn(III) oxidation state.

Interestingly, the calculated electron affinities of the **1-N-oxo_a** and **1-N-oxo_b** isomers are 5.26 and 5.37 eV, respectively, which is smaller than the 6.99 eV value for species **1-oxo**, and this implies that the **N-oxo** species are much weaker oxidants than the **1-oxo** species.

Finally, since both **2-N-oxo** isomers are energetically highly (about 30−50 kcal/mol) unfavorable relative to **2-oxo**, we will not discuss them in detail.

$[Imd(OSalen)Mn(III)]^+$ (1-Imd-N-oxo) and [Imd(OSalen)Mn(II)] (2-Imd-N-oxo) Species. As seen in Table 2, the coordination of the imidazole ligand only slightly changes the barrier heights separating the **1-Imd-oxo** species from the **1-Imd-N-oxo** species. Specifically, transition states, **TS-1-Imd-N-oxo_a** and **TS-1-Imd-N-oxo_b**, lie 20.3 and 20.6 kcal/mol above the quintet **1-Imd-oxo** species, respectively. Normal coordinate analysis shows that these transition states each have one imaginary frequency of 732i and 691i cm^{-1} for **TS-1-Imd-N-oxo_a** and **TS-1-Imd-N-oxo_b**, respectively. Comparison of the geometrical parameters of the transition states **TS-1-Imd-N-oxo** and **TS-1-N-oxo** shows that they are very similar, while the former could be regarded as a later TS compared to the latter. Indeed, as seen from Table 3, the forming O^3−N^1 and O^3−N^2 bond lengths in **TS-1-Imd-N-oxo_a** and **TS-1-Imd-N-oxo_b** are both 1.74 Å as opposed to 1.81 and 1.85 Å in **TS-1-N-oxo**, respectively.

Despite the similarity in the transition state structures, we found that the addition of the imidazole ligand significantly affects the geometry of the product **Imd-N-oxo_a**, but not **Imd-N-oxo_b**. To confirm this observation, we ran a 20 point intrinsic reaction coordinate (IRC[69]) calculation with 0.1 Å step size from **TS-1-Imd-N-oxo_a** toward the product **1-Imd-N-oxo_a**, followed by full optimization. The IRC calculation demonstrates that at first the insertion of O^3 into Mn$-N^1$ takes place, and then simultaneously N^4-Mn$-O^3$ and O^1-Mn$-O^2$ angles start widening, which leads to the **1-Imd-N-oxo_a** structure, depicted in Figure 2. Presumably, such rearrangement is triggered by the strain in the two adjacent six- and seven-member rings sharing the Mn$-O^3-N^1$ fragment, which arises from the push-effect on O^3 due to the imidazole ligand. As a result, complex **1-Imd-N-oxo_a** adopts a square pyramidal configuration with a new basal plane composed of O^1, O^2, O^3, and N^4. In contrast, in the case of **1-Imd-N-oxo_b** the structure formed upon insertion does not undergo further rearrangement, presumably due to the fact that under the imidazole push-effect, strain in the six-member ring in the boat conformation does not allow the oxygen to occupy the vertical position.

Structures of **2-Imd-N-oxo_a** and **2-Imd-N-oxo_b** were optimized starting from the structures of corresponding **1-Imd-N-oxo**. We believe that several other isomers may exist for any of the two structures described; however, we did not attempt here to locate all of them but rather studied those arising from located transition states **TS-1-Imd-N-oxo_a** and **TS-1-Imd-N-oxo_b**.

[(OSalen)Mn(III)]$^+$ (1-Peroxo) and [(OSalen)Mn(II)] (2-Peroxo). Although the **peroxo** isomers of the species **1** and **2** do not have immediate analogues in metal porphyrins, we present our results for **peroxo** species, because they have similar genealogy as the **N-oxo** isomers described in the the previous section.

As discussed already, the **peroxo** isomers could be the products of insertion of the O^3-atom into one of the two basal Mn$-$O bonds (Mn$-O^1$ or Mn$-O^2$) and could have two different forms, **a** and **b**, similar to those in the **N-oxo** case (see Scheme 1). Since lower-spin states are found to be significantly unfavorable for **N-oxo** as well as for **peroxo** isomers of **1** and **2** (Table 2), we will briefly discuss only high-spin states of the **peroxo** isomers of **1** and **2**.

As seen in Table 2, the **peroxo** isomers of cationic species **1**, **1-peroxo_a** and **1-peroxo_b**, lie 14$-$16 kcal/mol higher in their high-spin states relative to the ^{3}A state of the complex **1-oxo**. In the case of neutral species **2**, energy differences between the lowest electronic states of **2-oxo** and **2-peroxo_a** and **2-peroxo_b** isomers are even larger, 51$-$53 kcal/mol. Since the **peroxo** isomers of **1** and **2** are energetically highly unfavorable, here we will not discuss their geometries, as well as transition states separating them from the corresponding oxo-species. They are most likely irrelevant to the olefin epoxidation.

[(Salen)Mn(V)N] (3). The isoelectronic nitrido analogue of the **1-oxo** species, **[(Salen)Mn(V)N]**, also could have singlet ^{1}A, triplet ^{3}A, and quintet ^{5}A electronic states. As seen in Table 2, the ^{1}A state is found to be ground state, and ^{3}A and ^{5}A states lie about 21.7 and 39.2 kcal/mol higher, respectively. These results are consistent with available experimental data, which show that the singlet ^{1}A state is the ground state[12,18,19,70] for complex **3**. Furthermore, the calculated important geometrical parameters of **3** are in excellent agreement with the available X-ray experiment[11,71] (see Table 3).

The molecular orbital correlation diagram of **3** (Figure 1F) is similar to that of **1-oxo**. The major difference is that in the ^{1}A state of **3** the $\delta(d_{x^2-y^2} + S_{SALC})$ orbital resides above both π- and σ-orbitals, while in the ^{3}A state it descends below the π-orbital but still remains above the σ-orbital, and it becomes lower than π- and σ-orbitals only in the ^{5}A state. Therefore, formal electronic configurations for the ^{1}A, ^{3}A, and ^{5}A states of **3** are $[\sigma(d_{z^2} + p_z(O^3))]^2[\pi(d_{xz} + p_x(O^3))]^2$-$[\pi(d_{yz} + p_y(O^3))]^2[\delta(d_{x^2-y^2} + S_{SALC})]^2[\delta(d_{x^2-y^2} - S_{SALC})]^2$, $[\sigma$-$(d_{z^2} + p_z(O^3))]^2[\delta(d_{x^2-y^2} + S_{SALC})]^2[\pi(d_{xz} + p_x(O^3))]^2[\pi(d_{yz} + p_y(O^3))]^2[\delta(d_{x^2-y^2} - S_{SALC})]^1[\pi^*(d_{xz} - p_x(O^3))]^1$, and $[\delta(d_{x^2-y^2} + S_{SALC})]^2[\sigma(d_{z^2} + p_z(O^3))]^2[\pi(d_{xz} + p_x(O^3))]^2$-$[\pi(d_{yz} + p_y(O^3))]^1[\delta(d_{x^2-y^2} - S_{SALC})]^1[\pi^*(d_{xz} - p_x(O^3))]^1$-$[\pi^*(d_{yz} - p_y(O^3))]^1$, respectively.

On the basis of the correlation MO diagram (Figure 1F), the formal bond orders of the terminal Mn$-N^3$ bond are assigned to be 3, $^5/_2$, and $^3/_2$ for ^{1}A, ^{3}A, and ^{5}A states, respectively. This observation is in exceptional agreement with the calculated Mn$-N^3$ bond lengths, which increase in the order 1.51 Å (^{1}A) < 1.64 Å (^{3}A) < 1.86 Å (^{5}A). Furthermore, the displacement of Mn atom from the basal plane, Mn$-P^3$, decreases in the order 0.51 Å (^{1}A) < 0.36 Å (^{3}A) < 0.17 Å (^{5}A), although the N^3-P^3 distance stays at the same values, 2.01, 1.99, and 2.02 Å.

Vibrational frequency analysis shows that the terminal Mn$-N^3$ bond stretching frequencies for species **3** are 1210 and 725 cm^{-1} for the ^{1}A and ^{3}A states, respectively, and have almost pure stretching character. However, for the ^{5}A state we have found three vibrations, 585, 608, and 614 cm^{-1}, which coupled the Mn$-N^3$ bond stretching with the in-plane motions of the basal plane atoms and the ethylenediamine bridge in symmetric and antisymmetric ways. Note that the calculated stretching frequency for the ^{1}A is higher than the experimentally established value 1047 cm^{-1},[11,18] which could be due to the deficiency of the BS1 used in these calculations.

B. Theoretical NMR ^{1}H, ^{13}C, ^{15}N, and ^{17}O Chemical Shifts. In this section, we compare the calculated NMR properties of the **1-oxo** and **3** nitrido species, which could facilitate assignments of the experimentally observed signals. Since the current methodology for calculation of NMR chemical shifts of transition metal complexes is limited to diamagnetic closed shell molecules,[72] our results are restricted

---

(69) Gonzalez, C.; Schlegel, H. B. *J. Chem. Phys.* **1989**, *90*, 2154$-$2161. Gonzalez, C.; Schlegel, H. B. *J. Chem. Phys.* **1990**, *94*, 5523$-$5527.

(70) Du Bois, J.; Tomooka, C. S.; Hong, J.; Carreira, E. M.; Day, M. W. *Angew. Chem., Int. Ed. Engl.* **1997**, *36*, 1645$-$1647.

(71) Allen, F. H.; Kennard, O. *Chem. Des. Autom. News* **1993**, *8*, 1, 31$-$37.

(72) Schreckenbach, G.; Ziegler, T. *Theor. Chem. Acc.* **1998**, *99*, 71$-$82. Kaupp, M.; Malkin, V. G.; Malkina, O. L. In *Encyclopedia of Computational Chemistry*; Schleyer, P. v. R., Ed.; John Wiley & Sons Inc.: Chichester, U.K., 1998; Vol. 3. Helgaker, T.; Jaszunski, M.; Ruud, K. *Chem. Rev.* **1999**, *99*, 293$-$352.

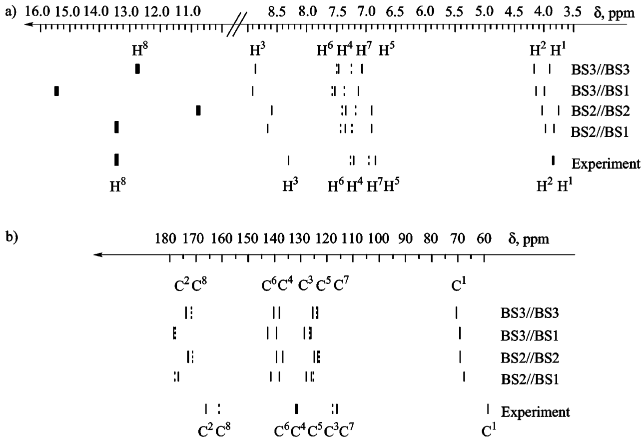

Figure 3. (a) ^{1}H and (b) ^{13}C NMR chemical shifts for H_2Salen calculated at the different levels of theory. All calculations were performed within the C_i symmetry constraint.

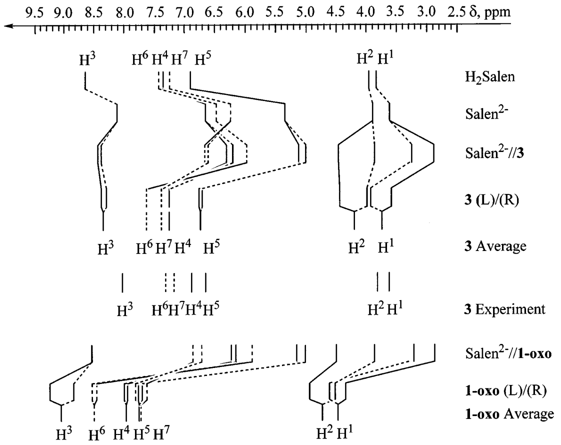

Figure 4. Genealogical representation of calculated ^{1}H chemical shifts. Letters L and R in parentheses refer to the left and right parts of the Salen fragment, and A is the average between the two. Solid lines connect signals from the left part of the molecule, whereas dashed lines connect right part signals.

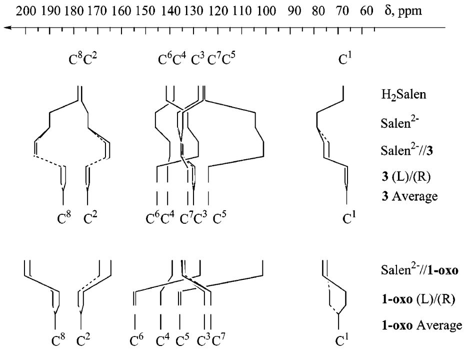

Figure 5. Genealogical representation of calculated ^{13}C chemical shifts. Letters L and R in parentheses refer to the left and right parts of the Salen fragment, and A is the average between the two. Solid lines connect signals from the left part of the molecule, whereas dashed lines connect right part signals.

to singlet-spin states of the mentioned species. Throughout this section, we exploit the labeling system given in Scheme 3 to refer to particular atoms in the molecules under investigation. The obtained results are presented in Figures 3−5 and Tables 4−6.

Prior to the NMR chemical shift calculations for the ^{1}A states of **1-oxo** and **3** species, we, once again, tested the performance of the B3LYP/BS1 method in the geometry optimization. For this purpose, we have optimized geometry of the H_2Salen molecule within the C_i symmetry constraint. As seen from Table 4S, the optimized structure is in good agreement with the X-ray results:[71,73] the root-mean-square error is found to be 0.12 Å with maximum deviation of 0.19 Å for 20 heavy atoms. Optimizations of H_2Salen with the BS2 and BS3 basis sets give almost identical results, except for some shorter bond lengths. The most affected are the heteroatomic bonds $C^1-N^1(N^2)$, $N^1(N^2)-C^2$, $C^8-O^1(O^2)$, and $O^1(O^2)-H$,[8] which shrink by 0.017, 0.027, 0.026, and 0.041 Å, respectively (see Table 4S for more details). Otherwise, improvement of the basis sets from BS1 to BS2 and BS3 has a negligible effect on the calculated geometries of H_2Salen. From these results for H_2Salen, and comparison of calculated and experimental data for species **3** presented in Table 2, we may conclude that the B3LYP/BS1 method provides satisfactory agreement with experiment in the geometry optimization in this particular system.

For ^{1}H chemical shifts (see Table 4 and Figure 3a) in H_2Salen, we have found that all approaches used in this paper, BS2//BS1 (BS2 for NMR chemical shift calculations, and BS1 for optimized geometry), BS2//BS2, BS3//BS1, and BS3//BS3, give similar results, which only differ in H^8 chemical shift. As expected, the larger basis set BS3//BS1 predicts more deshielded chemical shifts;[64] however, BS2//BS1 calculated values agree with the available experimental ^{1}H NMR chemical shifts[74] better than those obtained with BS3//BS1.

As seen in Table 5 and Figure 3b, for the ^{13}C chemical shift[75] of H_2Salen, the picture of the dependence on the used basis sets is moderate, although at BS3//BS1, the C^2 and C^8 and C^5 and C^7 swap places in the spectrum relative to BS2//BS1. Overall, the BS3//BS1 approach results in stronger deshielding of ^{13}C chemical shifts. Not surprisingly,[64] ^{15}N and ^{17}O chemical shifts for H_2Salen demonstrate stronger basis set dependence (see Table 6) and, thus, must be taken with caution. However, the presented results justify the use of the BS2//BS1 approach to study NMR chemical shifts of **1-oxo** and **3**. Therefore, in the following paragraphs, we discuss chemical shifts calculated at the BS2//BS1 level.

To investigate the chemical shifts in the species **1-oxo** and **3**, as well as to determine the origins of possible differences between those, we decided to perform a genealogical analysis. In this analysis, we utilized the following scheme. At first, we doubly deprotonate H_2Salen to get the Salen^{2-} unit, which is common for both **1-oxo** and **3**, and calculate NMR ^{1}H, ^{13}C, ^{15}N, and ^{17}O chemical shifts for the free Salen^{2-} fragment. Then, we deform the Salen^{2-} fragment into the geometry in the complexes **1-oxo** and **3**, calculate NMR ^{1}H, ^{13}C, ^{15}N, and ^{17}O chemical shifts for “deformed” Salen^{2-} fragments, and compare the calculated chemical

---

(73) Bresciani Pahor, N.; Calligaris, M.; Nardin, G.; Randaccio, L. *Acta Crystallogr., Sect. B: Struct. Crystallogr. Cryst. Chem.* **1978**, *34*, 1360−1363.

(74) Kuska, H. A.; Gause, E. P. *Spectrochim. Acta* **1986**, *42A*, 1331−1332.

(75) Bremser, W. *Carbon-13 NMR Spectral Data: A “Living” Com-microfiche collection of reference material*, 4th ed.; VCH: Weinham, 1987.

Table 4. ^{1}H NMR Chemical Shifts (ppm) for the Singlet Molecules Calculated Relative to TMS[a]

species	method	H^1	H^2	H^3	H^4	H^5	H^6	H^7	H^8
H_2Salen	exptl[b]	3.85	3.85	8.30	7.18	6.84	7.26	6.95	13.2
	BS2//BS1	3.82	3.99	8.66	7.37	6.91	7.45	7.26	13.41
	BS3//BS1	3.98	4.15	8.91	7.53	7.14	7.57	7.38	15.49
	BS2//BS2	3.76	4.04	8.59	7.35	6.89	7.41	7.18	10.81
	BS3//BS3	3.91	4.19	8.84	7.47	7.08	7.50	7.26	12.76
Salen^{2-}	BS2//BS1	3.60	3.95	8.16	6.68	5.35	6.49	6.23	
1-oxo(L)	BS2/BS1	4.35/2.86	4.93/4.50	9.24/8.52	7.99/6.22	7.75/5.14	8.45/5.88	7.61/6.85	
1-oxo(R)		4.61/3.21	4.51/3.86	8.82/8.52	7.93/6.14	7.69/5.01	8.53/5.88	7.8/6.70	
1-oxo(A)		4.48/3.03	4.72/4.18	9.03/8.52	7.96/6.18	7.72/5.08	8.49/5.88	7.71/6.78	
3	exptl[c]	3.66	3.81	8.01	6.89	6.65	7.32	7.19	
3(L)	BS2//BS1	3.59/2.90	4.44/4.46	8.39/8.43	7.27/6.30	6.76/5.13	7.62/5.99	7.38/6.67	
3(R)		3.93/3.24	4.00/3.87	8.30/8.38	7.26/6.21	6.70/5.00	7.63/5.99	7.39/6.62	
3(A)		3.76/3.07	4.22/4.16	8.34/8.36	7.26/6.25	6.73/5.06	7.63/5.99	7.38/6.64	

[a] Letters L, R, and A in parentheses designate left and right parts of the molecule and average between the two, respectively. Values after slash refer to chemical shifts of demetalated Salen^{2-} at the geometry in the corresponding complex. [b] Ref 74. [c] Ref 17.

Table 5. ^{13}C NMR Chemical Shifts (ppm) for the Singlet Molecules Calculated Relative to TMS[a]

species	method	C^1	C^2	C^3	C^4	C^5	C^6	C^7	C^8
H_2Salen	exptl[b]	59.6	166.5	116.8	131.5	118.6	132.3	116.8	161.0
	BS2//BS1	68.2	177.4	128.0	138.3	125.8	142.0	126.1	178.1
	BS3//BS1	69.6	178.5	128.7	139.6	127.1	142.9	126.7	178.4
	BS2//BS2	68.9	172.9	125.0	137.4	123.5	139.4	123.7	171.6
	BS3//BS3	70.2	174.1	125.6	138.3	124.4	140.2	124.2	172.2
Salen^{2-}	BS2//BS1	78.8	173.6	137.2	146.5	104.7	132.7	134.5	190.3
1-oxo(L)	BS2//BS1	67.5/76.1	176.4/164.8	126.7/134.8	143.7/138.7	136.8/102.2	154.0/127.6	123.1/134.6	186.6/200.8
1-oxo(R)		72.9/74.8	177.9/169.2	126.6/135.1	143.5/138.8	136.0/102.0	155.1/127.9	123.5/133.8	188.7/198.8
1-oxo(A)		70.2/75.5	177.1/167.0	126.6/135.0	143.6/138.8	136.4/102.1	154.5/127.8	123.3/134.2	187.6/199.8
3(L)	BS2//BS1	66.5/ 75.7	174.1/165.0	129.4/134.8	141.4/139.9	124.0/101.5	145.5/128.1	132.1/135.5	183.7/196.4
3(R)		67.1/73.6	175.0/167.5	130.6/135.1	141.4/139.8	123.8/101.5	145.3/128.1	131.9/135.2	185.2/195.8
3(A)		66.8/74.6	174.5/166.8	130.0/135.0	141.4/139.9	123.9/101.5	145.4/128.1	132.0/135.4	184.4/196.1

[a] Letters L, R, and A in parentheses designate left and right parts of the molecule and average between the two, respectively. Values after slash refer to chemical shifts of demetalated Salen^{2-} in the geometry of the corresponding complex. [b] Ref 75.

Table 6. ^{15}N and ^{17}O NMR Chemical Shifts for the Singlet Molecules Calculated Relative to NH_3 and CH_3OH[a]

species	method	N^1	N^2	O^1	O^2	N^3/O^3
H_2Salen	BS2//BS1	328.1	328.1	146.6	146.6	
	BS3//BS1	331.6	331.6	150.8	150.8	
	BS2//BS2	322.1	322.1	133.8	133.8	
	BS3//BS3	323.8	323.8	139.7	139.7	
Salen^{2-}	BS2//BS1	376.1	376.1	405.4	405.4	
1-oxo	BS2//BS1	306.7/440.7	295.0/437.2	494.0/614.0	458.6/629.3	1769.6
3	BS2//BS1	258.9/426.8	246.7/422.4	233.2/578.1	235.7/583.2	1393.9

[a] Values after slash refer to chemical shifts of demetalated Salen^{2-} in the geometry of the corresponding complex.

shifts with those of free Salen^{2-}. Last, we insert into the Salen^{2-} fragment the corresponding MnX fragments of **1-oxo** and **3** and, again, calculate chemical shifts. This can be formulated as follows, for instance, for species **3**:

$$\delta(3) = \delta(\mathrm{H_2Salen}) + [\delta(\mathrm{Salen}^{2-}) - \delta(\mathrm{H_2Salen})] + [\delta(\mathrm{Salen}^{2-}//\mathbf{3}) - \delta(\mathrm{Salen}^{2-})] + [\delta(\mathbf{3}) - \delta(\mathrm{Salen}^{2-}//\mathbf{3})]$$

Such a scheme allows us to separate the geometry deformation and electronic effects associated with the MnX fragments.

^{1}H NMR. As seen in Figure 4, upon deprotonation of H_2Salen, ^{1}H chemical shifts become more shielded due to uncompensated negative charge in Salen^{2-} anion. Protons of the benzene rings are shielded the most, imine protons are shielded moderately, and ethylene bridge protons are shielded the least. Deformation of the Salen^{2-} fragment to its geometry in **1-oxo** deshields the aromatic H^7, imine H^3, and mean ethylene bridge H^2, while shielding the rest of the protons further. Upon introduction of the MnO^3 fragment, strong deshielding occurs on H^5 and H^6, among the aromatic protons. Ethylene bridge protons H^1 experience a strong deshielding effect, while H^2 is only modestly deshielded. Imine protons H^3 also become modestly deshielded. Overall, the formation of **1-oxo** results in deshielding of all proton signals relative to H_2Salen due to total positive charge of the complex. As a result, the positions of the H^5 and H^7 proton signals are swapped.

In the case of **3**, deformation of Salen^{2-} preserves the pattern of displacements (Figure 4). Protons H^3, H^7, and H^2 are deshielded slightly less, whereas H^4, H^6, and H^1 are shielded less than in the case of **1-oxo**. Introduction of the MnN^3 fragment renders the molecule neutral. As a result, benzene protons H^6 and H^7 become deshielded relative to H_2Salen, whereas H^4 and H^5 protons, on the contrary, become slightly more shielded, which results in swapping H^4 and H^7 protons. Imine protons H^3 and ethylene bridge H^1 also become more shielded, while H^2 becomes deshielded in **3**.

^{13}C NMR. We note that ^{13}C NMR spectra of the studied molecules are composed of three different groups of signals, namely group 1, ethylene bridge carbons (C^1), group 2, two carbons connected with electronegative atoms (C^2 and C^8), and group 3, aromatic carbons (C^3-C^7). As seen from Figure 5, upon deprotonation of the H_2Salen ethylene bridge C^1, group 2 C^8 and aromatic group 3 C^3, C^4, and C^7 become deshielded, whereas group 2 C^2, and aromatic C^5 and C^6 on the opposite, become more shielded relative to H^2Salen. Deformation of Salen^{2-} into the geometry of **1-oxo** deshields aromatic C^7 and group 2 C^8 and shields the other carbons. Introduction of the MnO^3 fragment strongly deshields aromatic C^5 and C^6 and also moderately deshields group 2 C^2 and aromatic C^4 signals, while it shields the rest of the signals relative to the deformed fragment. Relative to H_2-Salen, ethylene bridge C^1 is deshielded by 2.0 ppm, group 2 C^2 and C^8 are shielded by 0.3 ppm and deshielded by 9.5 ppm, respectively, and aromatic carbons C^4, C^5, and C^6 are deshielded by 5.3, 10.6, and 12.5 ppm and C^3 and C^7 are shielded by 1.4 and 2.8 ppm, respectively. Overall, this results in swapping C^5 and the pair of C^3 and C^7 carbons.

Deformation of the Salen^{2-} fragment into the geometry of **3** preserves the pattern of displacements, with C^2 and C^8 being deshielded less than in **1-oxo**. Introduction of the MnN^3 fragment strongly deshields group 2 C^2 and aromatic group 3 C^5 and C^6, but only moderately aromatic C;^{4} ethylene bridge C^1 and group 2 C^8 are strongly shielded, while aromatic C^3 and C^7 are shielded only modestly. Relative to H_2Salen, ethylene bridge C^1 is shielded by 1.4 ppm, group 2 C^2 and C^8 are shielded by 2.9 ppm and deshielded by 6.3 ppm, aromatic carbons C^3, C^4, C^6, and C^7 are deshielded by 2.0, 3.1, 3.4 and 5.9 ppm, and C^5 is shielded by 1.9 ppm, respectively. Overall, this results in swapping C^3 and C^7 signals. Comparing spectra of **1-oxo** to **3**, we note that ethylene bridge carbon C^1 is deshielded by 3.4 ppm; group 2 carbons C^2 and C^8 are deshielded by 2.6 and 3.2 ppm, respectively, and group 3 carbons C^4, C^5, and C^6 are deshielded by 2.2, 12.5, and 9.1 ppm, while C^3 and C^7 are more shielded by 3.4 and 8.7 ppm, respectively.

^{15}N and ^{17}O NMR. ^{15}N and ^{17}O chemical shifts would be the most sensitive to deprotonation, deformation, and MnX fragment coordination. Indeed, as shown in Table 6, deprotonation of H_2Salen results in strong shielding of the ^{15}N by 48 ppm and ^{17}O by 258 ppm. Deformation of the Salen^{2-} fragment into the geometry of **1-oxo** shields N^1 and N^2 further by 64.6 and 61.1 ppm (by 62.8 ppm on average), as well as O^1 and O^2 by 208.6 and 223.9 ppm (by 216.2 ppm on average), respectively. MnO^3 fragment coordination strongly deshields N^1 and N^2 by 134.0 and 142.2 ppm (by 138.1 ppm on average), but shields O^1 and O^2 by 120 and 170.7 ppm (by 145.3 ppm on average), respectively. In the case of **3**, the situation is qualitatively the same, but the effects are larger. Thus, deformation of the Salen^{2-} fragment results in less shielding as compared to **1-oxo** (41.8 and 46.2 ppm for N^1 and N^2, and 172.7 and 177.8 ppm for O^1 and O^2, respectively). Introduction of the MnN^3 fragment causes larger deshielding of 209.7 and 222.0 ppm for N^1 and N^2, and larger shielding 344.9 and 347.5 ppm for O^1 and O^2, respectively. Finally, the terminal oxygen in **1-oxo** is highly deshielded at 1769.6 ppm, whereas terminal nitrogen in **3** shows strongly deshielded chemical shift of 1393.9 ppm.

IV. Conclusions

From this discussion we can draw the following conclusions: (1) For the cationic **1-oxo** species, the ^{1}A, ^{3}A, and ^{5}A states are virtually degenerate in energy, while for the neutral **2-oxo** species, the ground ^{4}A state lies 6.4 kcal/mol lower than ^{2}A. In contrast to **1-oxo**, in the isoelectronic nitrido species **3**, the ^{1}A state is well separated from the triplet and quintet states and is the ground state, which is in agreement with available experimental data.[12,18,19,70] (2) We have investigated the isomerization of **1-oxo** and **2-oxo** species into corresponding **N-oxo** and **peroxo** isomers. For cationic species **1**, it has been shown that **1-N-oxo** isomers in their ground ^{5}A states are more stable (by 10−12 kcal/mol) than the **1-oxo** isomer, with corresponding intramolecular insertion barriers of 21−22 kcal/mol relative to **1-oxo**. This indicates that **1-oxo** species are kinetically stable toward collapse into the **N-oxo** species. The **1-peroxo** isomers are calculated to be 14−16 kcal/mol higher than the **1-oxo** isomer. For neutral species **2**, the **2-N-oxo** and **2-peroxo** isomers lie significantly higher in energy (by 25−30 and 50−52 kcal/mol, respectively) than the **2-oxo** isomer. (3) Introduction of an axial imidazole ligand destabilizes the low-spin states, ^{1}A and ^{3}A, and ^{2}A, of **1-oxo** and **2-oxo** species, respectively. As a result, the ^{3}A and ^{5}A states of **1-Imd-oxo** become even closer to each other in energy. Moreover, the ^{1}A state of **1-Imd-oxo** and ^{2}A state of **2-Imd-oxo** become much higher in energy than the corresponding high-spin states. Furthermore, introduction of the imidazole ligand slightly stabilizes **N-oxo** isomers, while it does not significantly change barrier heights separating **N-oxo** and **oxo** isomers. (4) The ^{1}H, ^{13}C, ^{15}N, and ^{17}O NMR chemical shift calculations for singlet **H_2Salen**, **1-oxo**, and **3** enable us to tentatively predict spectra of the unstable **1-oxo** species. From these calculations, we concluded that the MnX fragment determines the difference in the chemical shifts between **1-oxo** and **3** species. In general, the MnO fragment results in more deshielded chemical shifts than MnN for all nuclei. (5) We further elaborate on the applicability of the B3LYP, B3P86, BLYP, BP86, and conventional Hartree−Fock (HF) methods to studies of the energy difference between low-lying spin states of **1-oxo** species. It was shown that hybrid functional methods (B3LYP and B3P86) stabilize high-spin states compared to pure density functional methods (BLYP and BP86). The source of this difference in the calculated energy gaps between the low-lying states at the hybrid and pure density functional levels is found to be the HF contribution; the HF method dramatically stabilizes high-spin states.

Acknowledgment. We thank Dr. Dmitry Khoroshun for fruitful discussions.The present research is in part supported by a grant (CHE-0209660) from the National Science Foundation. Acknowledgment is made to the Cherry L. Emerson Center of Emory University for the use of its resources, which is in part supported by a National Science Foundation grant (CHE-0079627) and an IBM Shared University Research Award.

Supporting Information Available: Tables 1S, 2S, and 3S describing selected molecular planes and related distances, calculated atomic spin densities, and Mulliken charges, respectively, Table 4S showing the geometries of H_2Salen calculated at the different level of theory, Table 5S listing Cartesian coordinates of all calculated species, and Table 6S showing their total, zero-point corrected and Gibbs free energies. This material is available free of charge via the Internet at http://pubs.acs.org.

IC026094Q